Received 2016 Sept 20
Preprint typeset using LaTeX style emulateapj v. 5/2/11

arXiv:1609.09490v1 [astro-ph.HE] 29 Sep 2016

MEASURING THE INNERMOST STABLE CIRCULAR ORBITS OF SUPERMASSIVE BLACK HOLES

G. Chartas[1,2], H. Krawczynski[3], L. Zalesky[1], C. S. Kochanek[4,5], X. Dai[6], C. W. Morgan[7], and A. Mosquera[7]

Received 2016 Sept 20

ABSTRACT

We present a promising new technique, the g-distribution method, for measuring the inclination angle (i), the innermost stable circular orbit (ISCO), and the spin of a supermassive black hole. The g-distribution method uses measurements of the energy shifts in the relativistic iron line emitted by the accretion disk of a supermassive black hole due to microlensing by stars in a foreground galaxy relative to the g-distribution shifts predicted from microlensing caustic calculations. We apply the method to the gravitationally lensed quasars RX J1131−1231 ($z_s = 0.658$, $z_l = 0.295$), QJ 0158−4325 ($z_s = 1.294$, $z_l = 0.317$), and SDSS 1004+4112 ($z_s = 1.734$, $z_l = 0.68$). For RX J1131−1231 our initial results indicate that $r_{\rm ISCO} \lesssim 8.5$ gravitational radii ($r_{\rm g}$) and $i \gtrsim 76^{\circ}$. We detect two shifted Fe lines, in several observations, as predicted in our numerical simulations of caustic crossings. The current ΔE-distribution of RX J1131−1231 is sparsely sampled but further X-ray monitoring of RX J1131−1231 and other lensed quasars will provide improved constraints on the inclination angles, ISCO radii and spins of the black holes of distant quasars.

Subject headings: galaxies: active — accretion, accretion disks — black hole physics — gravitational lensing: micro — gravitational lensing: strong — quasars: individual (RX J1131−1231, QJ 0158−4325, SDSS 1004+4112)

1. INTRODUCTION

One technique for measuring the innermost stable circular orbit (ISCO) and spin parameter a ($a = Jc/GM_{BH}^2$, where J is the angular momentum) of AGN relies on modeling the relativistically blurred Fe Kα fluorescence lines originating from the inner parts of the disk (e.g., Fabian et al. 1989; Laor 1991; Reynolds & Nowak 2003). This relativistic iron line method can only be applied to a few relatively bright nearby Seyferts where the line is detectable with a high signal-to-noise ratio. Even then, the Fe Kα line in most Seyferts is typically very weak, and constraining the spin and accretion disk parameters of Seyferts requires considerable observing time on *XMM-Newton* and *Chandra*. Moreover, the accuracy of the relativistic Fe line method for constraining the spin of a black hole from the broadened red wing of the Fe line profile is also questioned (e.g., Miller et al 2009; Sim et al. 2012). However, 3–50 keV observations with *NuSTAR*, such as the recent observations of Mrk 335 that indicate a spin parameter of > 0.9 at 3 σ confidence, can help to constrain the reflection component and better distinguish between models (Parker et al. 2014). Most of the measured spin parameters in Seyfert galaxies are found to be $\gtrsim 0.9$ (e.g., Reynolds 2014 and references therein). This may be the result of a selection bias in flux-limited samples (Vasudevan et al. 2016). For example, recent observations and simulations (Fabian 2014, Keck et al. 2015, Vasudevan et al. 2016) suggest that rapidly spinning black holes will tend to have stronger reflected relative to direct X-ray emission, making it easier to measure the spin parameter in these objects.

The relativistic iron line method has been applied to the gravitationally lensed quasars RX J1131−1231 (Reis et al. 2014) and Q2237+0305 (Reynolds et al. 2014) and well as to a stacked spectrum of 27 lensed $1.0 < z < 4.5$ quasars observed with *Chandra* (Walton et al. 2015). Specifically, the relativistic disk reflection features were fit with standard relativistic Fe Kα models to infer inclination angles and spin parameters of $i = 15^{\circ}{}^{+9^{\circ}}_{-15^{\circ}}$ and $a = 0.87^{+0.08}_{-0.15}$ for RX J1131−1231 (Reis et al. 2014) and $i \lesssim 11.5^{\circ}$ and $a = 0.74^{+0.06}_{-0.03}$ for Q2237+0305 (Reynolds et al. 2014).

These studies have not, however, correctly accounted for the effects of gravitational microlensing. Gravitational microlensing is a well studied phenomenon in lensed quasars (e.g., see the review by Wambsganss 2006 and references therein) where stars near the lensed images produce time variable magnification of source components whose amplitude depends on the location and size of the emission region. In particular, in our analysis of the X-ray spectra of lensed quasars (Chartas et al. 2016), we have frequently observed structural changes in the Fe Kα emission indicating that the line emission is being differentially microlensed. Thus, applying the rel-

[1] Department of Physics and Astronomy, College of Charleston, Charleston, SC, 29424, USA, chartasg@cofc.edu
[2] Department of Physics and Astronomy, University of South Carolina, Columbia, SC, 29208
[3] Physics Department and McDonnell Center for the Space Sciences, Washington University in St. Louis, 1 Brookings Drive, CB 1105, St. Louis, MO 63130, USA
[4] Department of Astronomy, The Ohio State University, 140 West 18th Avenue, Columbus, OH 43210, USA
[5] Center for Cosmology and AstroParticle Physics, The Ohio State University, 191 W. Woodruff Avenue, Columbus, OH 43210, USA
[6] Homer L. Dodge Department of Physics and Astronomy, University of Oklahoma, Norman, OK 73019, USA
[7] Physics Department, United States Naval Academy, Annapolis, MD 21403, USA

ativistic Fe Kα line method to stacked spectra of lensed quasars, without accurately accounting for microlensing, is likely to lead to unreliable and unrealistic results.

In Section 2 we present the X-ray observations and analyses of the *Chandra* observations of RX J1131−1231, QJ 0158−4325, and SDSS 1004+4112. In Section 3 we discuss our recently developed technique based on microlensing to provide a robust constraint on the inclination angle, the location of the ISCO, and the spin parameter, and present an analytic estimate of the fractional energy shifts $g = E_{\rm obs}/E_{\rm rest}$ and numerical simulations of microlensing events. In Section 4 we present our results from modeling the observed distribution of g and the distribution of the measured energy separations of shifted Fe Kα lines in cases where two shifted lines are detected in an individual spectrum. Finally, in Section 5 we rule out several alternative scenarios to explain the shifted iron lines and present a summary of our conclusions. Throughout this paper we adopt a flat Λ cosmology with $H_0 = 67$ km s^{-1} Mpc^{-1} $\Omega_\Lambda = 0.69$, and $\Omega_{\rm M} = 0.31$ (Planck Collaboration et al. 2013).

2. X-RAY OBSERVATION AND DATA ANALYSIS

We have performed multiwavelength monitoring of several gravitationally lensed quasars (e.g., see Table 1 of Chartas et al. 2016 and references within) with the main scientific goal of measuring the emission structure near the black holes in the optical, UV, and X-ray bands in order to test accretion disk models. The X-ray monitoring observations were performed with the *Chandra X-ray Observatory* (hereafter *Chandra*). The Optical (B, R and I band) observations were made with the SMARTS Consortium 1.3m telescope in Chile. The UV observations were performed with the *Hubble Space Telescope*. In this paper we focus on constraining the inclination angles, ISCO radii, and spin parameters of quasars RX J1131−1231, QJ 0158−4325, and SDSS 1004+4112 using the *Chandra* observations of these objects.

RX J1131−1231 (hereafter RXJ1131) was observed with the Advanced CCD Imaging Spectrometer (ACIS; Garmire 2003) on board the *Chandra X-ray Observatory* 38 times between 2004 April 12 and 2014 July 12. Results from the analysis of observations 1–6 of RXJ1131 were presented in Chartas et al. (2009), and Dai et al. (2010) and those for observations 7–29 are in Chartas et al. (2012). Results from the analysis of a subset of these observations have also been presented in Blackburne et al. (2006), Kochanek et al. (2007), and Pooley et al. (2012). Here we describe the data analysis for the remaining 9 observations, but we will use the results from all 38 observations in our microlensing analysis. QJ 0158−4325 (hereafter QJ0158) was observed with ACIS 12 times between 2010 November 6 and 2015 June 10, and SDSS 1004+4112 (hereafter SDSS1004) was observed with ACIS 10 times between 2005 January 1 and 2014 June 2. Results from the analysis of the first 6 observations of QJ0158, and the first 5 observations of SDSS1004 were presented in Chen et al. (2012).

We re-analyzed all the *Chandra* observations of RXJ1131, QJ0158, and SDSS1004 using the software CIAO 4.8 with CALDB version 4.7.2, provided by the *Chandra X-ray Center* (CXC). A log of the observations for each object in our study that includes observation dates, observation identification numbers, exposure times, ACIS frame times and the observed 0.2–10 keV counts are presented in Tables 1, 2, and 3. We used standard CXC threads to screen the data for status, grade, and time intervals of acceptable aspect solution and background levels.

In Figures 1, 2, and 3 we show the 0.2–10 keV light-curves of the images of RXJ1131, QJ0158, and SDSS1004. The light-curves have been shifted by the time-delays estimated by Tewes et al. (2012), Faure et al. (2009), and Fohlmeister et al. (2008), respectively. Microlensing will affect the images differently resulting in uncorrelated variability between images. Large uncorrelated events are noticeably present in the images of RXJ1131, QJ0158, and SDSS1004, indicating that the X-ray emission regions are significantly smaller than the projected Einstein radius of the stars and thus affected by microlensing (e.g., Chartas et al. 1995, 2009; Dai et al. 2003, 2010; Blackburne et al. 2006; Pooley 2007; Mosquera et al. 2013)

For the spectral analyses, we followed the approach described in Chartas et al. (2012). We extracted events from circular regions with radii of 1.5 arcsec slightly off-center from the images to reduce contamination from nearby images. The backgrounds were determined by extracting events within an annulus centered on the mean location of the images with inner and outer radii of 7.5 arcsec and 50 arcsec, respectively. Spectral fits were restricted to events with energies between 0.4–10 keV. Spectra with fewer than ~ 200 counts were fit using the C-statistic (Cash 1979)[8], as appropriate for fitting spectra with low S/N. Spectra with larger number of counts were fit using both the C and χ^2 statistics.

We fit the *Chandra* spectra for each epoch with a model that consists of a power law with neutral intrinsic absorption at the redshift of the source. Galactic column densities in the directions of RXJ1131, QJ0158, and SDSS1004 were fixed to $N_H = 3.60 \times 10^{20}$ cm^{-2}, $N_H = 1.88 \times 10^{20}$ cm^{-2}, and $N_H = 1.13 \times 10^{20}$ cm^{-2}, respectively (Dickey & Lockman 1990). Measurements of the differential X-ray absorption between images in lensed quasars SBS 0909+523, FBQS 0951+2635, and B 1152+199 by Dai & Kochanek (2009) have been used to successfully constrain the dust-to-gas ratio of the lens galaxies and we plan to present the application of this method to our lens sample in a future paper. We next added one or two Gaussian emission lines to the model and tested for the significance of the added line/s. The significance of the emission lines was determined by varying the energy and width of the iron line and its flux to calculate the χ^2 of the fit as a function of the Fe line energy and iron line flux. In several cases two emission lines are detected in a single spectrum. We record all cases where one or more emission lines are detected above the 90%, and 99% confidence levels. Note that all these lines are detected in single epochs and not from stacked observations.

In Figures 4, 5, and 6 we show typical examples of Fe Kα lines detected in the spectra of individual images and epochs from RXJ1131, QJ0158, and SDSS1004, respectively. We also show the respective χ^2 contours of the detected lines. Tables 5, 6, and 7 provide the line and continuum properties for all these detections. For RX J1131 we have 78 line detections out of the 152 spectra

[8] The spectra were binned to have at least one count per bin.

(38 epochs × 4 images) at > 90% confidence, of which 21 lines are detected at > 99% confidence. For the 6 *Chandra* observations of QJ0158 with exposure times of ∼19 ks, we detect 10 iron lines in 12 spectra (6 epochs × 2 images) at > 90% confidence, of which 3 iron lines are detected at > 99% confidence. For the 10 *Chandra* observations of SDSS1004, we detect the iron line in 8 out of the 40 spectra (10 epochs × 4 images) at > 90% confidence, of which 6 iron lines are detected at > 99% confidence. For several closely separated observations we detect energy shifts of the Fe Kα line in consecutive and closely separated epochs most likely produced by the same caustic crossing. For example, Figure 5 shows a likely caustic crossing in QJ0158 during December 2013.

In Figure 7 we show the generalized Doppler shift parameter g of the Fe line as a function of the equivalent width (EW) of the iron line in RXJ1131. We find a correlation between g and the EW with a Kendall's rank correlation coefficient of $\tau = 0.28$ significant at > 99.9% confidence. One possible explanation of this correlation is that blueshifted line emission is Doppler boosted, resulting in the observed equivalent widths of the blueshifted lines being larger than the redshifted lines.

In Figure 8 we show the flux of the Fe line as a function of the flux of the continuum, where the line flux is the normalization of the Gaussian line component of the best-fit model, and the continuum flux is the normalization of the power-law component of the best-fit model calculated at 1 keV. We find a strong correlation between the line and continuum fluxes, with a Kendall's rank correlation coefficient of $\tau = 0.5$ that is significant at > 99.9% confidence. The relative flux of the X-ray continuum to the Fe Kα line flux depends on a variety of accretion disk parameters and geometries including the emissivity profile of the disk, the distance of the caustic from the black hole, the geometry of the corona, the geometry of the disk emission, the caustic crossing angle and the inclination angle. Variations of the X-ray continuum and the Fe Kα line flux during caustic crossing have been simulated in Popovic et al. (2006) for a variety of accretion disk parameters and geometries. These simulations indicate that once the magnification caustic has passed over the black hole, the microlensing magnifications of the line and continuum regions are similar and both the line and continuum decay in a similar manner with distance from the black hole. This may explain part of the observed correlation between these quantities.

3. THE G- AND ΔE-DISTRIBUTIONS

We have recently developed a new technique based on microlensing that provides a robust constraint on the disk inclination angle and on the location of the ISCO, which in turn may provide an estimate of the spin of the black hole. Our technique is very simple. The stars near each lensed image produce magnification patterns with a characteristic Einstein radius of

$$R_{\rm E} = D_{\rm OS}\left[\frac{4G\langle M\rangle}{c^2}\frac{D_{\rm LS}}{D_{\rm OL}D_{\rm OS}}\right]^{1/2} \quad (1)$$

where $\langle M\rangle$ is the mean mass of the lensing stars, the $D_{\rm ij}$ are the angular diameter distances, and the subscripts L, S, and O refer to the lens, source, and observer, respectively.

These patterns contain caustic curves on which the magnification diverges. As the observer, lens and source move, the quasar experiences a time varying magnification whose amplitude is determined by the size of the source, with larger sources showing lower amplitudes because they more heavily smooth the magnification patterns (e.g., Wyithe et al. 2000, 2002, Kochanek 2004). If the X-ray emission is dominated by the inner edge of the disk, then the characteristic source size is $r_{\rm s} \sim 10r_{\rm g} \sim 10^{15}(M_{\rm BH}/10^9{\rm M}_\odot)$ cm where $r_{\rm g} = {\rm G}M_{\rm BH}/{\rm c}^2$. The effective source velocity across the pattern for our three quasars ranges between $v_{\rm e} \sim 600 - 785$ km/s (see Mosquera & Kochanek 2011) leading to two characteristic time scales for variability: the Einstein crossing time R_E/v_e, typically several years, and the source crossing time $r_{\rm s}/v_e$, typically a few months (see Table 1).

As a caustic crosses the accretion disk it differentially magnifies the Fe Kα line emission to produce changes in the line profile. We will observe these as shifts in the line energy which we use to calculate the distribution of the fractional energy shifts g=$E_{\rm obs}/E_{\rm rest}$ (the "g-distribution"). We first present an analytic estimate of the energy shift of the iron line caused by microlensing and compare these analytic estimates with the observed energy shifts. Numerical simulations of microlensing events are presented later on in the section. The observed energy, $E_{\rm obs}$, of a photon emitted near the event horizon of a supermassive black hole will be shifted with respect to the emitted rest-frame energy, $E_{\rm emit}$, due to general relativistic and Doppler effects. The ratio between the observed energy and the emitted rest-frame energy is often referred to as the generalized Doppler shift and defined as

$$g = \frac{E_{obs}}{E_{emit}} = \delta\sqrt{\frac{\Sigma\Delta}{\rm A}} \quad (2)$$

where the Doppler factor δ is

$$\delta = \sqrt{\frac{1-v_\phi^2}{1-v_\phi\cos\theta_c}} \quad (3)$$

$A = \left(r^2+a^2\right)^2 - a^2\Delta\sin^2\theta$, $\Sigma = r^2+a^2\sin^2\theta$, and $\Delta = r^2-2r_g r + a^2$, where θ_c is the angle between the direction of the orbital velocity v_ϕ of the emitting plasma and our line of sight neglecting the general relativistic effect of the bending of the photon trajectories and relativistic aberration (see appendix for details). In §4 we compare our analytic estimate of the generalized Doppler factor g with the observed limits of the g-distributions of RXJ1131.

We next use numerical simulations to evaluate if the microlensing of the X-ray emission from a mass accreting supermassive black hole can indeed produce energy spectra similar to the observed ones. The simulations assume that RXJ1131 accretes through a standard geometrically thin, optically thick accretion disk (Shakura & Sunyaev 1973; Novikov & Thorne 1973) described by the analytical general relativistic equations of Page & Thorne (1974). This assumption seems to be well justified for two reasons. Sluse et al. (2012) estimate that the black hole of RXJ1131 has a mass $M_{\rm BH}$ between 8×10^7 $M_\odot$ and 2×10^8 $M_\odot$ and a bolometric luminosity of $L_{\rm Bol} \approx$

10^{45} erg s^{-1}. The inferred ratio of $L_{\rm Bol}/L_{\rm Edd}$ is therefore expected to range between $0.01 - 0.42$. It is therefore likely that RXJ1131 is accreting in the regime in which accretion is believed to be dominated by a geometrically thin, optically thick accretion disk (see e.g. the discussion in McKinney et al. 2014). General relativistic (radiation) magnetohydrodynamical simulations indicate that the analytical equations describe accretion disks reasonably accurately (Noble et al. 2011; Kulkarni et al. 2011; Penna et al. 2012; Sadowski 2016). However, optical/UV observations of microlensing events in quasars indicate that accretion disks are larger than predicted by thin disk theory (Morgan et al. 2010), and similar discrepancies are found using measurements of continuum lags in the nearby Seyferts NGC2617 (Shappee et al. 2014) and NGC5548 (Edelson et al. 2015; Fausnaugh et al. 2016).

We use a general relativistic ray tracing code (Krawczynski 2012; Hoormann et al. 2016; Beheshtipour et al. 2016) to track photons of initially unspecified energy from a lamppost corona (Matt et al. 1991) to the observer, accounting for the possibility that the photons impinge on the accretion disk and either reflect or prompt the emission of Fe-Kα photons. The compactness of the corona has been observationally and independently confirmed via microlensing (e.g., Pooley et al. 2007; Chartas et al. 2009, 2016; Dai et al. 2010; Morgan et al. 2008; Mosquera et al. 2013; Blackburne et al. 2014, 2015; MacLeod et al. 2015) and reverberation studies (Fabian et al. 2009; De Marco et al. 2011; Kara et al. 2013, 2016; Cackett et al. 2014; Emmanoulopoulos et al. 2014; Uttley et al. 2014). The reverberation studies in many cases constrain the distance between the corona and central black hole to lie in the range of $3 - 10 r_g$.

In our simulations the corona is located above the black hole at a radial Boyer Lindquist (BL) coordinate $r = 5\,r_{\rm g}$ slightly offset from the polar axis ($\theta = 10^{\circ}$), and emits isotropically in its rest frame. The 0-component of the wavevector k^{μ} of the photon packet is proportional to the energies of the photons, and we assume that the corona emits a power-law SED with a photon number power law of $dN/dE \propto E^{-\Gamma}$ with $\Gamma = 1.75$. After transforming the photon packet's wavevector into the global BL coordinates, the code integrates the geodesic equation until the photon packet either comes too close to the black hole horizon (when we assume it will enter the black hole), impinges on the accretion disk, or arrives at a fiducial stationary observer at $r_{\rm obs} = 10,000\,r_{\rm g}$.

We assume that the accretion disk extends from the innermost stable circular orbit (ISCO) to 100 $r_{\rm g}$. We use simple prescriptions for treating the absorption, reflection and reprocessing in the disk's photosphere. If a photon packet hits the disk it is absorbed with probability $p_{\rm abs}$, it scatters with probability $p_{\rm es} = (1-p_{\rm abs})R/(1+R)$, or it prompts the emission of a monoenergetic Fe-Kα photon with probability $p_{\rm Fe-K\alpha} = (1 - p_{\rm abs})/(1 + R)$, so that $p_{\rm es}/p_{\rm Fe-K\alpha} = R$. Although we use $p_{\rm abs} = 0.9$ and $R = 1$, the results do not depend strongly on the specific choice (see Ross & Fabian 2005; García et al. 2013, for more detailed treatments). The Fe-Kα photons are always emitted with an energy of 6.4 keV in the rest frame of the accretion disk with a statistical weight that depends on the net redshift or blueshift g incurred between the emission of the photon in the corona and its absorption in the accretion disk. More specifically, the weight is given by $w = g^{\Gamma-1}$ with

$$g = \frac{u_{\hat{\mu}} k^{\hat{\mu}}}{u_{\check{\mu}} k^{\check{\mu}}}. \tag{4}$$

Here $u^{\check{\mu}}$ and $u^{\hat{\mu}}$ denote the four velocities of the corona and the accretion disk plasmas, respectively, and $k^{\check{\mu}}$ and $k^{\hat{\mu}}$ denote the photon packet wave vectors in the rest frames of the corona plasma and accretion disk plasma (before the absorption of the photon packet), respectively. The scattering model is based on the classical treatment by Chandrasekhar (1960) of scattering by an indefinitely deep electron atmosphere. Tracking photon packets forward in time allows us to model multiple interactions of the photon packets with the accretion disk before or after a photon packet prompts the emission of a Fe-Kα photon packet (see also Schnittman & Krolik 2009, 2010, and references therein). Our treatment neglects the possibility that Fe-Kα photons return to the accretion disk and may prompt the emission of another Fe-Kα photon, but this is a very small correction. When a photon packet reaches the observer, its wavevector is transformed from the global BL frame into the reference frame of a coordinate stationary observer. Although we simulated 10 million photon packets for a range of black hole spins ($a = 0, 0.1, 0.2, ..., 0.9, 0.95, 0.98, 0.998$) we will show here only exemplary results for $a = 0.3$. The results for other black hole spins will be presented in a forthcoming paper (Krawczynski et al. 2016).

In this paper we use the general parameterization of the microlensing magnification μ close to caustic folds above the magnification μ_0 outside of the caustic (see e.g. Schneider et al. 1992; Chen et al. 2013):

$$\mu \,=\, 1 + \frac{K}{\mu_0 \sqrt{y_{\perp}}} H(y_{\perp}) \tag{5}$$

with $y_{\perp}$ giving the position of the origin of the emission in the source plane along a coordinate axis perpendicular to the fold, K is the caustic amplification factor, and H is the Heaviside function (i.e. $H(y_{\perp}) = 0$ for $y_{\perp} < 0$ and $H(y_{\perp}) = 1$ for $y_{\perp} \geq 0$). For microlensing by a random field of stars K/μ_0 is given by (Witt et al. 1993; Chartas et al. 2002)

$$K/\mu_0 \,\approx\, \beta \sqrt{\zeta_{\rm E}} \tag{6}$$

where β is a constant of order unity and $\zeta_{\rm E}$ is the Einstein radius for stars of average mass $\langle M \rangle$. In this paper, we show results for $\beta = 0.5$ and $\zeta_{\rm E} = 1640\,r_{\rm g}$, corresponding to $\langle M \rangle = 0.25 M_{\odot}$ and $M_{\rm BH} = 10^8 M_{\odot}$. For each simulated black hole spin, we simulate caustic crossings at crossing angles θ_c (the angle between the normal of the caustic fold and the black hole spin axis) between 0 and 360° in 20° steps and for $-30\,r_{\rm g}$ to $+30\,r_{\rm g}$ offsets of the caustic from the center of the black hole. An angle of $\theta_c = 0$ corresponds to a caustic fold perpendicular to the black hole spin axis with the positive side of the caustic (the side with $\mu > 1$) pointing in the $\theta = 0$ direction.

The left panel of Figure 9 shows a 2-D map of the surface brightness of the Fe-Kα line emission in the source plane after convolving it with a caustic magnification ($a = 0.3$, $i = 82.5^{\circ}$, $\theta_c = \pi/2$). An actual observer would see a different surface brightness distribution, as Figure

9 accounts for the flux magnification but not for the image distortion caused by the gravitational lensing. The magnification pattern of Equation (5) can clearly be recognized by a sudden jump from $\mu = 1$ to $\mu \gg 1$ followed by the gradual return of the magnification to $\mu \approx 1$. The right panel shows the resulting Fe-Kα energy spectrum. Similar to the *Chandra* energy spectra shown in Figure 4, the simulated energy spectrum exhibits two distinct peaks. Scrutinizing similar maps and energy spectra for different caustic crossing angles and offsets reveals that double peaks appear naturally (but not only) when the positive side of the caustic magnifies lower surface brightness emission which is not as strongly Doppler boosted as the emission from the portions of the accretion disk approaching the observer with a speed close to the speed of light. Figure 10 shows a 2-D map of the g-factors of the Fe-Kα photons for the same parameters as Figure 9. The image clearly shows the highest blueshifts from regions of the accretion disk moving towards us with a speed close to the speed of light. Note that the gravitational redshift wins over the Doppler blueshift very close to the event horizon. The minimum and maximum g-values are 0.42 and 1.4, respectively, and are in good agreement with the observed values.

We analyzed the energy spectra for all caustic crossing angles and offsets with an algorithm identifying the most prominent peaks and fitting them with Gaussians. The algorithm first finds the highest peak in the photon number energy spectrum (dN/dE) and then searches for an additional peak which rises more than 10% above the valley between the two peaks. Figure 11 shows the distribution of all the peak energies found in this way (singles and doubles). Figure 12 presents all simulated and observed double peak energies. Although a statistical analysis of the results is outside the scope of this paper, we will see in §4 that the simulated results do resemble the observed ones at least on a qualitative level.

4. RESULTS

We detect shifted and broadened Fe Kα lines in almost every image of RXJ1131 that has an exposure time of >20 ks as shown in Figure 4 and Table 5. Relativistically broadened Fe Kα lines detected in the spectra of unlensed AGN are produced from emission originating from the entire inner accretion disk. In contrast, the microlensed Fe Kα lines in the spectra of lensed AGN are produced from a relatively smaller region on the disk that is magnified as a microlensing caustic crosses the disk. We therefore expect microlensed Fe Kα lines to be in general narrower and with larger equivalent widths that those detected in unlensed AGN.

The presence of these energy shifts is evidence that most of the shifted iron line emission detected in RXJ1131 does not originate from reflection from a torus or other distant material but from material near the event horizon of the black hole. The evolution of the energy and shape of the Fe Kα line during a caustic crossing depends on the ISCO, spin, inclination angle of the disk and caustic angle. The extreme shifts are produced when the microlensing caustic is near the ISCO of the black hole. Measurements of the distribution of the fractional energy shifts $g = E_{\rm obs}/E_{\rm rest}$ of the Fe Kα line due to microlensing therefore provide a powerful limit on the g-distribution that can be used to estimate the ISCO, spin and inclination angle of the disk.

In Figure 13 we show the g-distribution (multiplied by the rest-frame energy of the Fe Kα line, $E_{\rm rest} = 6.4$ keV) of the Fe Kα lines with $> 90\%$ and $>99\%$ detections in RXJ1131 for all images and epochs. One important feature of this iron line energy-shift distribution is the significant limits of the distribution at rest-frame energies of $E_{\rm min} = 3.78^{+0.16}_{-0.10}$ keV and $E_{\rm max} = 8.24^{-0.48}_{+0.15}$ keV, where the the error bars for both $E_{\rm min}$ and $E_{\rm max}$ are at the 90% confidence level, for iron lines detected at $> 90\%$ confidence. These limits represent the most extremely redshifted and blueshifted Fe Kα lines. If we interpret the largest energy-shifts as being due to X-ray emission originating close to the ISCO, we obtain upper limits on the size of the ISCO and inclination angle of RXJ1131. In Figure 14 we show the g-distribution for the individual images of RXJ1131. The apparent differences of the distributions between images can be a result of several factors including the differences in the frequency of microlensing along different lines of sight, the differences in the S/N of the spectra (D being the faintest image) and differences in caustic crossing angles. The observed g-distributions of Figures 13 and 14 closely resemble the simulated distribution of all peaks shown in Figure 11.

The energy of photons emitted from a ring at the ISCO are bounded by maximum and minimum values, $g_{\rm max}$ and $g_{\rm min}$, of the generalized Doppler shift. The maximum blueshift of the Fe line places a constraint on the inclination angle. Specifically, for RXJ1131 the measured generalized Doppler factor $g_{\rm max} = 1.29 \pm 0.04$ (90% confidence) constrains the inclination angle to be $\gtrsim 64°$, for any values of the spin parameter and caustic crossing angle, as shown in Figure 15, assuming that the thin accretion disc extends all the way down to the ISCO. If we also require that the measured $g_{\rm min}$ and $g_{\rm max}$ shifts are produced by photons emitted from the same radius, then the inclination angle is required to be $i \gtrsim 76°$ for photons emitted from a radius of $r \sim 8.5\ r_g$ for any values of the spin parameter and caustic crossing angle, as also shown in Figure 15. We conclude that the current observed values of $g_{\rm min}$ and $g_{\rm max}$ place an upper limit on the ISCO radius of $r_{\rm ISCO} \lesssim 8.5 r_{\rm g}$ and a disk inclination angle of $i \gtrsim 76°$.

We also detect energy shifts in the Fe line in QJ0158 and SDSS1004, but they have not been monitored as frequently as RXJ1131. In Figure 16 we show the g-distributions of the Fe Kα lines with $> 90\%$ confidence detections in QJ0158 and SDSS1004 for all images and epochs. These g-distributions of QJ0158 and SDSS1004 are too sparsely populated to provide statistically significant constraints on the ISCO radii with the available data but demonstrate that these lenses also have microlensed Fe emission.

In several observations we detect two shifted Fe lines, as shown in Figures 4 and 5. Specifically, the number of detected double lines in the spectra of images A, B, C, and D of RXJ1131 are 9, 5, 3, 0, respectively. All the cases are detected at the $> 90\%$ confidence level. In the following, we call energy spectra with one peak "singles" and energy spectra with two peaks "doubles". We searched for possible correlations between the energies of the doubles. A moderately significant correlation, with

a Kendall's rank correlation coefficient of $\tau = 0.6$, and a significance of $> 98\%$ confidence, is detected between the observed $E_{\rm min}$ and $E_{\rm max}$ values in image A. The observed energies of the double lines detected in the spectra of image A and the spectra of all images are shown in Figures 17 and 18, respectively. We performed a straight-line least-squares fit to the data with the FITEXY routine (Press et al. 1992), which takes into account errors in both coordinates. Based on the magnification maps of RX J1131−1231 (see Figures 4-6 of Dai et al. 2010) we expect a limited range of caustic crossing angles over $\sim$ 10 years. Any change in the caustic crossing angle over time will contribute to the scatter in the observed $E_{\rm min}$ and $E_{\rm max}$ values of doubles. The scatter in the $E_{\rm min}$ and $E_{\rm max}$ values detected in all images is even larger, as we would expect from the differences in the caustic structures and their directions of motion in different images (Kendall's $\tau = 0.4$, significant at $> 97\%$ confidence).

In Figure 19 we show the $\Delta E-$distribution of the rest-frame energy separations for the Fe line pairs detected in all images of RXJ1131 at the $> 90\%$ confidence level, where $\Delta E = E_{\rm max} - E_{\rm min}$ and $E_{\rm max}$, $E_{\rm min}$ are the rest-frame energies of the shifted lines. As we discussed in §3, our numerical simulations show that the peak energy of the $\Delta E-$distribution depends strongly on the spin parameter. Specifically, our simulations indicate that the ΔE-distributions of RX J1131−1231 for input spin parameters of $a = 0$ and $a = 0.98$ peak at 1.8 ± 0.2 keV and 3.2 ± 0.2 keV, respectively. We find that the maximum of the observed ΔE-distribution of RX J1131−1231 peaks at $\sim 3.5 \pm 0.2$ keV, implying a spin parameter of $a \gtrsim 0.8$. Additional observations of RXJ1131 will provide more representative and complete g and ΔE-distributions and place tighter constraints on the disk inclination angle, the ISCO radius and the spin.

5. DISCUSSION AND CONCLUSIONS

Our systematic spectral analysis of all the available *Chandra* observations of lensed quasars RXJ1131, QJ0158, and SDSS1004 has revealed the presence of a significant fraction of lines blueshifted and redshifted with respect to the energy of the expected Fe Kα fluorescent line. We interpret these energy shifts as being the result of ongoing microlensing in all the images. This seems logical given the prior detections of microlensing of the optical/UV (e.g., Blackburne et al. 2006; Morgan 2008; Fohlmeister et al. 2007; Fian et al. 2016, Motta et al. 2012) and X-ray continuum (e.g., Chartas et al. 2009, 2012, 2016; Dai et al. 2010; Chen et al. 2012) in all three sources. We consider several alternative scenarios and examine whether they can explain the observed shifted iron lines.

(a) *Non-microlensed emission from hot-spots and patches from an inhomogeneous disk.*
Redshifted Fe emission lines have been reported in observations of a few bright Seyfert galaxies (i.e., Iwasawa et al. 2004; Turner et al. 2004, 2006; Miller et al. 2006; Tombesi et al. 2007). Correlated modulation of redshifted Fe line emission and the continuum were reported in NGC 3783 (Tombesi et al. 2007). Specifically, the spectrum of NGC 3783 shows, in addition to a core Fe Kα line at 6.4 keV, a weaker redshifted wing and redshifted Fe emission line component. The redshifted line and wing appear to show an intensity modulation on a 27 ks timescale similar to that of the 0.3-10 keV continuum. Tombesi et al. (2007) argue that the lack of Fe line energy modulation disfavors the orbiting flare/spot interpretation for NGC 3783. We note that the relative intensity of the core Fe line to the redshifted Fe line component in NGC 3783 is about a factor of 9. The core Fe Kα line has an equivalent width of about 120 eV and the redshifted line of $\sim$13 eV. Redshifted lines are also reported to be present in the spectrum of Mrk 766 (Turner et al. 2004; 2006), where a weak component of the Fe line with an equivalent width of 15^{+6}_{-5} eV shows a periodic variation of photon energy. The proposed scenario by Turner et al. (2006) is that the energy variation is caused by a hot spot on the disk within $\sim 100\ r_{\rm g}$ orbiting with a period of about $\sim$ 165 ks. The average spectrum of Mrk 766 shows a broad iron line centre near 6.7 keV with an equivalent width of about 90 eV (possibly from reflection off an ionized disk) and a narrower component at 6.4keV (possibly from reflection from distant material).

The shifted Fe lines detected in our gravitationally lensed quasar sample have very different properties from those reported in NGC 3783 and Mrk 766 while our our microlensing interpretation is consistent with the observed properties of the energy shifted lines. Specifically, the equivalent widths of the energy shifted lines in the lensed quasar sample range from EW = 500 eV to 3,000 eV compared to the EW=13 eV and EW=15 eV in the shifted lines detected in NGC 3783 and Mrk 766, respectively. Non-microlensed emission from hot-spots and patches from an inhomogeneous disk lie below the detection threshold of the individual spectra of the lensed quasars. The non-microlensed emission from the Fe Kα line at 6.4 keV is not detected in individual spectra of RX J1131−1231, but is detected in the stacked spectra of RX J1131−1231 with E = $6.36^{+0.07}_{-0.08}$ keV and EW = 154^{+70}_{-80} eV (Chartas et al. 2012, 2016). In the cases of Seyfert galaxies NGC 3783 and Mrk 766 the redshifted weak Fe lines are always accompanied by a significantly stronger core component near 6.4 keV whereas this is not the case for the lensed quasars. Another point supporting the microlensing interpretation is the detection of a significant number of double lines in RX J1131−1231, as predicted in our numerical simulations of magnification caustics crossing an accretion disk. The intensities of these doubles are not consistent with non-microlensed Fe emission from hot-spots and patches from an inhomogeneous disk.

(b) *Possible intrinsic absorption mimicking two apparent lines in RX J1131−1231.*
Our analysis of the 4×38 spectra of RX J1131−1231 does not find any significant intrinsic absorption of the continuum spectra (Chartas et al 2012) and there are no absorption lines detected in the spectra that contain doubles.

We conclude that the variability in the flux and energy of the iron line detected in the *Chandra* observations of RXJ1131, QJ0158, and SDSS1004 is due to ongoing microlensing of all the images.

Large magnification events are typically inferred from the departure of the time-delay corrected flux-ratios of images from a constant and images that show significant uncorrelated variability are significantly affected by

microlensing. We note, however, that a relatively large number of the shifted Fe lines were found in images that do not show significant variability of their flux ratios or significant uncorrelated variability. This implies that the line profiles found using stacked spectra taken over multiple epochs, even when excluding spectra from images that show variability of their flux ratios, are also distorted by microlensing and that applying the relativistic Fe Kα method as used to analyze local Seyferts will not lead to reliable results. Any apparent broadening of the iron line in a stacked spectrum of a lensed quasar is a combination of both microlensing and the relativistic blurring seen in unlensed Seyferts. The average stacked spectrum of a microlensed quasar differs significantly, especially near the Fe Kα line, from that of an unlensed one. The main reason for this difference is that the reflection and direct(coronal) components of a stacked spectrum of a microlensed quasar are not a simple uniform magnification of the reflection and direct components of a unlensed quasars. Caustic magnification patterns (e.g. see Figures $12-16$ of Kochanek 2004) move along a certain direction with respect to the source (that differs between images) and the caustic magnification is not uniform. Stacked spectra of lensed quasars will thus not result in uniformly magnified reflection and direct spectral components but will produce spectra that have been selectively magnified by caustics moving along a limited range of caustic crossing angles. The caustic magnification factor K will also vary between caustic crossings making the stacked spectrum deviate even more than a uniformly magnified quasar spectrum.

We summarize our main conclusions from the X-ray observations of RXJ1131, QJ0158, and SDSS1004 as follows:

(1) Redshifted and blueshifted Fe lines with rest-frame EWs ranging between 500 eV and 3,000 eV are detected in the individual epoch spectra of lensed quasars RXJ1131, QJ0158, and SDSS1004. We interpret these energy shifts as the result of microlensing of Fe line emission within $\sim 20\ r_{\rm g}$ of the black hole.

(2) The g-distribution of the observed energy shifts in RXJ1131 is compared to analytic and numerical models and both models provide similar constraints on accretion disk parameter. Specifically, the maximum value of $g_{\rm max}= 1.29^{+0.04}_{-0.04}$ constrains the inclination angle to be $i \gtrsim 76^{\circ}$ and the minimum value $g_{\rm min} = 0.59$ constrains $r_{\rm ISCO} \lesssim 8.5 r_g$. One of the strengths of the g-distribution method is that the energies of the shifted Fe lines are more robustly detected than the extreme weak red wings of the relativistic Fe Kα line that are found mostly in nearby Seyfert galaxies. For example, the energies of the shifted lines are not sensitive to the modeling of the underlying continuum, while, the shape of the relativistic Fe Kα red wing is very sensitive to the continuum model. The g-distribution method can be applied to infer the inclination angles, ISCO radii and spins of distant quasars where the relativistic Fe Kα red wing is typically to faint to constrain these parameters in distant quasars. One of the weaknesses of the g-distribution method is that there are additional model parameters related to describing the gravitational lens.

(3) Several spectra show two shifted Fe lines, which we refer to as doubles. The peak energies of the doubles are moderately correlated. Our numerical simulations reproduce the double lines during caustic crossings and we find that the distribution of the separations of the peak energies is strongly dependent on the spin parameter. The maximum of the observed ΔE-distribution of RX J1131$-$1231 peaks at $\sim 3.5 \pm 0.2$ keV suggesting a high spin parameter. Although a statistical analysis of the results still needs to be performed, inspection of the mean energy, peak energy, and shape of the distribution indicates a rather high value of the spin $a \gtrsim 0.8$. The available ΔE-distribution of RX J1131$-$1231 is sparsely populated and additional observations are required to better constrain the peak energy of this distribution and infer the spin parameter more accurately.

(4) We find several correlations in the microlensed spectra of RXJ1131 with results summarized in Table 8. Specifically, we find a correlation between the rest-frame equivalent width of the iron lines and the generalized Doppler shift parameter g of the iron line ($\tau = 0.28$, $P > 99.9\%$). The flux of the shifted Fe line is found to be correlated with the flux of the continuum for Fe Kα lines detected at $> 90\%$ confidence in all images of RXJ1131 ($\tau = 0.5$, $P > 99.9\%$). The energies of the doubles in image A are also found to be correlated ($\tau = 0.6$, $P > 98\%$).

(5) Our numerical simulations of microlensing caustic crossings reproduce the observed distribution of energy of single and double shifts in microlensed spectra, and predict the correlations observed in the spectra.

Scheduled future monitoring observations with *Chandra* of the lensed quasars RXJ1131, QJ0158, SDSS1004, and Q 2237+0305 with sufficiently long exposure times to improve the significance of the detections will provide more representative and complete distributions of the generalized Doppler shift g values of the Fe Kα line in these objects. The g-distribution method and modeling of doubles is expected to provide robust constraints on inclination angle, the ISCO radii and spins of the black holes of these distant lensed quasars. With the Large Synoptic Survey Telescope coming online in the near future we expect $\sim$ 4,000 new lensed systems to be discovered, opening up the possibility of measuring black hole and accretion disk parameters over a wide range of redhsifts and quasar Eddington ratios $L_{Bol}/L_{\rm Edd}$.

We acknowledge financial support from NASA via the Smithsonian Institution grants SAO GO4$-$15112X, GO3$-$14110A/B/C, GO2-13132C, GO1-12139C, and GO0-11121C. CWM gratefully acknowledges support from NSF Award AST-1211146. CSK is supported by NSF grant AST-1515876.

REFERENCES

Beheshtipour, B., Hoormann, J., Krawczynski, H. 2016, ApJ (in press).

Blackburne, J. A., Pooley, D., & Rappaport, S. 2006, ApJ, 640, 569

Blackburne, J. A., Kochanek, C. S., Chen, B., Dai, X., & Chartas, G. 2014, ApJ, 789, 125

Blackburne, J. A., Kochanek, C. S., Chen, B., Dai, X., & Chartas, G. 2015, ApJ, 798, 95

Cackett, E. M., Zoghbi, A., Reynolds, C., et al. 2014, MNRAS, 438, 2980

Chandrasekhar, S. 1960, New York: Dover, 1960

Chartas, G., Falco, E., Forman, W., et al. 1995, ApJ, 445, 140

Chartas, G., Agol, E., Eracleous, M., et al. 2002, ApJ, 568, 509

Chartas, G., Kochanek, C. S., Dai, X., Poindexter, S., & Garmire, G. 2009, ApJ, 693, 174

Chartas, G., Kochanek, C. S., Dai, X., et al. 2012, ApJ, 757, 137

Chartas, G., Rhea, C., Kochanek, C., et al. 2016, Astronomische Nachrichten, 337, 356

Chen, B., Dai, X., Kochanek, C. S., et al. 2011, ApJ, 740, L34

Chen, B., Dai, X., Kochanek, C. S., et al. 2012, ApJ, 755, 24

Dai, X., Chartas, G., Agol, E., Bautz, M. W., & Garmire, G. P. 2003, ApJ, 589, 100

Dai, X., & Kochanek, C. S. 2009, ApJ, 692, 677

Dai, X., Kochanek, C. S., Chartas, G., et al. 2010, ApJ, 709, 278

de Marco, B., Ponti, G., Uttley, P., et al. 2011, MNRAS, 417, L98

Emmanoulopoulos, D., Papadakis, I. E., Dovčiak, M., & McHardy, I. M. 2014, MNRAS, 439, 3931

Fabian, A. C., Rees, M. J., Stella, L., & White, N. E. 1989, MNRAS, 238, 729

Fabian, A. C., Zoghbi, A., Ross, R. R., et al. 2009, Nature, 459, 540

Fohlmeister, J., Kochanek, C. S., Falco, E. E., et al. 2007, ApJ, 662, 62

Fausnaugh, M. M., Denney, K. D., Barth, A. J., et al. 2016, ApJ, 821, 56

Fian, C., Mediavilla, E., Hanslmeier, A., et al. 2016, arXiv:1608.03831

García, J., Dauser, T., Reynolds, C. S., et al. 2013, ApJ, 768, 146

Hoormann, J. K., Beheshtipour, B., & Krawczynski, H. 2016, Phys. Rev. D, 93, 044020

Kara, E., Alston, W. N., Fabian, A. C., et al. 2016, MNRAS, 462, 511

Kara, E., Cackett, E. M., Fabian, A. C., Reynolds, C., & Uttley, P. 2014, MNRAS, 439, L26

Karas, V., & Sochora, V. 2010, ApJ, 725, 1507

Kerr, R. P. 1963, Physical Review Letters, 11, 237

Kochanek, C. S. 2004, ApJ, 605, 58

Kochanek, C. S., Dai, X., Morgan, C., Morgan, N., & Poindexter, S. C., G. 2007, Statistical Challenges in Modern Astronomy IV, 371, 43

Krawczynski, H. 2012, ApJ, 754, 133

Krawczynski, H., Chartas, G., Kislat, F., Beheshtipour, B. 2016, (in preparation).

Kulkarni, A. K., Penna, R. F., Shcherbakov, R. V., et al. 2011, MNRAS, 414, 1183

MacLeod, C. L., Morgan, C. W., Mosquera, A., et al. 2015, ApJ, 806, 258

Matt, G., Perola, G. C., & Piro, L. 1991, A&A, 247, 25

McKinney, J. C., Tchekhovskoy, A., Sadowski, A., & Narayan, R. 2014, MNRAS, 441, 3177

Mosquera, A. M., & Kochanek, C. S. 2011, ApJ, 738, 96

Mosquera, A. M., Kochanek, C. S., Chen, B., et al. 2013, ApJ, 769, 53

Motta, V., Mediavilla, E., Falco, E., & Muñoz, J. A. 2012, ApJ, 755, 82

Miller, L., Turner, T. J., & Reeves, J. N. 2009, MNRAS, 399, L69

Morgan, C. W., Kochanek, C. S., Dai, X., Morgan, N. D., & Falco, E. E. 2008, ApJ, 689, 755-761

Morgan, C. W., Kochanek, C. S., Morgan, N. D., & Falco, E. E. 2010, ApJ, 712, 1129

Morgan, C. W., Hainline, L. J., Chen, B., et al. 2012, ApJ, 756, 52

Mosquera, A. M., Kochanek, C. S., Chen, B., et al. 2013, ApJ, 769, 53

Müller, A., & Camenzind, M. 2004, A&A, 413, 861

Noble, S. C., Krolik, J. H., Schnittman, J. D., & Hawley, J. F. 2011, ApJ, 743, 115

Novikov, I. D., & Thorne, K. S. 1973, Black Holes (Les Astres Occlus), 343

Page, D. N., & Thorne, K. S. 1974, ApJ, 191, 499

Pooley, D., Blackburne, J. A., Rappaport, S., & Schechter, P. L. 2007, ApJ, 661, 19

Pooley, D., Rappaport, S., Blackburne, J. A., Schechter, P. L., & Wambsganss, J. 2012, ApJ, 744, 111

Parker, M. L., Wilkins, D. R., Fabian, A. C., et al. 2014, MNRAS, 443, 1723

Penna, R. F., Sądowski, A., & McKinney, J. C. 2012, MNRAS, 420, 684

Reis, R. C., Reynolds, M. T., Miller, J. M., & Walton, D. J. 2014, Nature, 507, 207

Reynolds, C. S. 2014, Space Sci. Rev., 183, 277

Reynolds, C. S., & Nowak, M. A. 2003, Phys. Rep., 377, 389

Reynolds, M. T., Walton, D. J., Miller, J. M., & Reis, R. C. 2014, ApJ, 792, L19

Ross, R. R., & Fabian, A. C. 2005, MNRAS, 358, 211

Sądowski, A. 2016, MNRAS, 459, 4397

Schneider, P., Ehlers, J., & Falco, E. E. 1992, Gravitational Lenses, XIV, 560 pp. 112 figs.. Springer-Verlag Berlin Heidelberg New York. Also Astronomy and Astrophysics Library, 112

Schnittman, J. D., & Krolik, J. H. 2010, ApJ, 712, 908

Schnittman, J. D., & Krolik, J. H. 2009, ApJ, 701, 1175

Shakura, N. I., & Sunyaev, R. A. 1973, A&A, 24, 337

Sluse, D., Hutsemékers, D., Courbin, F., Meylan, G., & Wambsganss, J. 2012, A&A, 544, A62

Uttley, P., Cackett, E. M., Fabian, A. C., Kara, E., & Wilkins, D. R. 2014, A&A Rev., 22, 72

Vasudevan, R. V., Fabian, A. C., Reynolds, C. S., et al. 2016, MNRAS, 458, 2012

Walton, D. J., Reynolds, M. T., Miller, J. M., et al. 2015, ApJ, 805, 161

Wambsganss, J. 2006, Saas-Fee Advanced Course 33: Gravitational Lensing: Strong, Weak and Micro, 453–540, arXiv:astro-ph/0604278

Witt, H. J., Kayser, R., & Refsdal, S. 1993, A&A, 268, 501

Wyithe, J. S. B., Agol, E., & Fluke, C. J. 2002, MNRAS, 331, 1041

Wyithe, J. S. B., Webster, R. L., & Turner, E. L. 2000, MNRAS, 318, 762

APPENDIX

CALCULATING THE GENERALIZED DOPPLER SHIFTS G

The generalized Doppler shifts g were calculated for the case of a spinning black hole (Kerr 1963) using the formalism described in Bardeen et al. (1972), Muller & Camenzind (2004), and Karas & Sochora (2010). The azimuthal velocity is

$$v_\phi = \tilde{\Omega}\frac{(\Omega - \Omega_0)}{\sqrt{\frac{\Delta\Sigma}{A}}} \tag{A1}$$

where $\tilde{\Omega}$ and Ω_0 are given by

$$\tilde{\Omega} = \sqrt{\frac{A}{\Sigma}}\sin\theta \quad \text{and} \tag{A2}$$

$$\Omega_0 = \frac{2a}{A}\frac{r}{r_g} \tag{A3}$$

For $r > r_{\rm ms}$ a Keplerian velocity profile is assumed and

$$\Omega = \frac{1}{(r/r_g)^{3/2} + a} \tag{A4}$$

For $r \leq r_{\rm ms}$ constant specific angular momentum is assumed and the angular velocity Ω is given by

$$\Omega = \Omega_0 + \frac{\Delta\Sigma}{A}\tilde{\Omega}^{-2}\frac{\lambda_{ms}}{1 - \Omega_0\lambda_{ms}} \tag{A5}$$

where

$$\lambda_{ms} = \frac{\widetilde{\Omega}^2_{ms}\left(\Omega_{ms} - \Omega_{0,ms}\right)}{\left[\left(\frac{\Delta\Sigma}{A}\right) + \Omega_{0,ms}\widetilde{\Omega}^2_{ms}\left(\Omega_{ms} - \Omega_{0,ms}\right)\right]} \tag{A6}$$

All quantities with the subscript ms are calculated at the marginal stable orbit.
For these calculations, we assumed the radial and toroidal velocity components v_r and v_θ of the radiating plasma of the accretion disk in the Zero Angular Momentum Observer frame to be relatively small. For a given inclination angle i, the angle between the direction of the orbital velocity v_ϕ of the plasma and our line of sight is assumed to range between a minimum and maximum value that will depend on the inclination angle i, and the angle between the caustic direction of motion and the projection of our line-of-sight onto the disk plane.

TABLE 1
Log of Observations of Quasar RX J1131−1231

Epoch	Observation Date	JD[a] (days)	*Chandra* Observation ID	Exposure Time (ks)	t_f[b] (s)	N_A[c] counts	N_B[c] counts	N_C[c] counts	N_D[c] counts
1	2004 April 12	3108	4814	10.0	3.14	425^{+22}_{-22}	2950^{+54}_{-54}	839^{+29}_{-29}	211^{+15}_{-15}
2	2006 March 10	3805	6913	4.9	0.741	393^{+20}_{-20}	624^{+25}_{-25}	204^{+14}_{-14}	103^{+10}_{-10}
3	2006 March 15	3810	6912	4.4	0.741	381^{+20}_{-20}	616^{+25}_{-25}	233^{+15}_{-15}	93^{+10}_{-10}
4	2006 April 12	3838	6914	4.9	0.741	413^{+20}_{-20}	507^{+23}_{-23}	146^{+12}_{-12}	131^{+12}_{-12}
5	2006 November 10	4050	6915	4.8	0.741	3708^{+61}_{-61}	1411^{+38}_{-38}	367^{+19}_{-19}	155^{+13}_{-13}
6	2006 November 13	4053	6916	4.8	0.741	3833^{+62}_{-62}	1618^{+40}_{-40}	415^{+20}_{-20}	115^{+11}_{-11}
7	2006 December 17	4087	7786	4.88	0.841	3541^{+102}_{-99}	1443^{+59}_{-58}	417^{+29}_{-28}	117^{+15}_{-13}
8	2007 January 01	4102	7785	4.70	0.441	2305^{+75}_{-74}	1082^{+51}_{-49}	312^{+26}_{-25}	108^{+15}_{-13}
9	2007 February 13	4145	7787	4.71	0.441	2451^{+79}_{-78}	1116^{+51}_{-49}	301^{+25}_{-24}	169^{+18}_{-17}
10	2007 February 18	4150	7788	4.43	0.441	2232^{+75}_{-73}	950^{+47}_{-45}	252^{+23}_{-22}	115^{+15}_{-14}
11	2007 April 16	4207	7789	4.71	0.441	2328^{+74}_{-74}	1202^{+54}_{-53}	344^{+27}_{-26}	99^{+14}_{-12}
12	2007 April 25	4216	7790	4.70	0.441	2043^{+67}_{-70}	1063^{+50}_{-48}	363^{+28}_{-26}	142^{+17}_{-16}
13	2007 June 04	4256	7791	4.66	0.441	2079^{+70}_{-69}	1480^{+60}_{-59}	373^{+28}_{-27}	108^{+15}_{-13}
14	2007 June 11	4263	7792	4.68	0.441	2254^{+73}_{-72}	1466^{+58}_{-56}	337^{+26}_{-25}	129^{+16}_{-15}
15	2007 July 24	4306	7793	4.67	0.441	1958^{+69}_{-68}	1324^{+57}_{-55}	353^{+27}_{-25}	81^{+12}_{-11}
16	2007 July 30	4312	7794	4.67	0.441	2725^{+80}_{-79}	1844^{+69}_{-67}	496^{+32}_{-31}	100^{+13}_{-12}
17	2008 March 16	4542	9180	14.32	0.741	5557^{+118}_{-117}	4347^{+105}_{-104}	1337^{+53}_{-51}	351^{+25}_{-24}
18	2008 April 13	4570	9181	14.35	0.741	8199^{+147}_{-147}	5654^{+118}_{-117}	1453^{+52}_{-52}	377^{+25}_{-24}
19	2008 April 23	4580	9237	14.31	0.741	6786^{+130}_{-130}	4927^{+112}_{-111}	1279^{+51}_{-51}	232^{+21}_{-20}
20	2008 June 01	4619	9238	14.24	0.741	4647^{+108}_{-106}	3252^{+90}_{-88}	878^{+43}_{-41}	463^{+28}_{-27}
21	2008 July 05	4653	9239	14.28	0.741	5587^{+119}_{-118}	3584^{+95}_{-94}	1001^{+44}_{-44}	635^{+33}_{-32}
22	2008 November 11	4782	9240	14.30	0.741	5135^{+115}_{-113}	3085^{+87}_{-85}	885^{+44}_{-42}	488^{+30}_{-29}
23	2009 November 28	5164	11540	27.52	0.741	36024^{+342}_{-340}	7357^{+126}_{-128}	2420^{+68}_{-68}	3827^{+82}_{-81}
24	2010 February 09	5237	11541	25.62	0.741	26850^{+281}_{-290}	5814^{+117}_{-117}	2059^{+86}_{-81}	2437^{+79}_{-88}
25	2010 April 17	5304	11542	25.67	0.741	20935^{+246}_{-245}	6124^{+120}_{-119}	1962^{+62}_{-62}	2813^{+70}_{-69}
26	2010 June 25	5373	11543	24.62	0.741	18521^{+230}_{-228}	5445^{+111}_{-111}	1522^{+54}_{-54}	1487^{+51}_{-51}
27	2010 November 11	5512	11544	25.56	0.741	27077^{+298}_{-467}	6316^{+120}_{-158}	1821^{+57}_{-64}	1730^{+56}_{-59}
28	2011 January 21	5583	11545	24.62	0.741	5689^{+153}_{-164}	3175^{+111}_{-123}	1008^{+47}_{-53}	982^{+47}_{-46}
29	2011 February 25	5618	12833	13.61	0.441	5412^{+159}_{-165}	4375^{+131}_{-128}	1161^{+52}_{-52}	821^{+44}_{-41}
30	2011 November 9	5875	12834	13.61	0.441	2206^{+77}_{-77}	2929^{+104}_{-104}	633^{+37}_{-37}	210^{+18}_{-18}
31	2012 April 11	6229	13962	13.67	0.441	2557^{+99}_{-99}	3660^{+107}_{-107}	730^{+39}_{-39}	480^{+27}_{-27}
32	2012 November 7	6239	13963	14.57	0.441	1521^{+73}_{-73}	2174^{+105}_{-105}	504^{+33}_{-33}	270^{+22}_{-22}
33	2012 November 18	6250	14507	9.13	0.441	738^{+59}_{-59}	1068^{+70}_{-70}	262^{+27}_{-27}	169^{+17}_{-17}
34	2012 December 12	6274	14508	9.13	0.441	1163^{+203}_{-73}	1518^{+98}_{-158}	399^{+34}_{-47}	187^{+49}_{-19}
35	2013 November 30	6627	14509	9.13	0.441	1420^{+100}_{-80}	1649^{+89}_{-111}	649^{+41}_{-44}	347^{+36}_{-29}
36	2014 January 3	6661	14510	8.75	0.441	1374^{+69}_{-76}	1344^{+88}_{-89}	441^{+32}_{-30}	322^{+34}_{-30}
37	2014 June 13	6822	14511	9.13	0.441	1352^{+75}_{-70}	1795^{+95}_{-122}	525^{+36}_{-36}	296^{+31}_{-26}
38	2014 July 7	6851	14512	10.04	0.441	806^{+76}_{-68}	1132^{+88}_{-92}	392^{+42}_{-42}	317^{+31}_{-29}

[a] Julian Date − 2450000. [b] ACIS frame-time. [c]Background-subtracted source counts for events with energies in the 0.2–10 keV band. The counts for images A and B of RX J1131−1231 are corrected for pile-up. Images C and D are not affected by pile-up.

TABLE 2
Log of Observations of Quasar Q J0158−4325

Epoch	Observation Date	JD[a] (days)	*Chandra* Observation ID	Exposure Time (ks)	t_f[b] (s)	$N_{soft,A}$[c] counts	$N_{soft,B}$[c] counts	$N_{hard,A}$[c] counts	$N_{hard,B}$[c] counts
1	2009 November 06	5142	11556	5.03	1.74	103±10	43±7	35±6	11±3
2	2010 January 12	5209	11557	5.02	1.74	125±11	61±8	35±6	19±4
3	2010 March 10	5266	11558	5.04	1.74	146±12	48±7	38±6	8±3
4	2010 May 23	5340	11559	4.94	1.74	131±11	38±6	38±6	10±3
5	2010 July 28	5406	11560	4.95	1.74	144±12	34±6	35±6	7±3
6	2010 October 06	5476	11561	4.94	1.74	122±11	39±6	28±5	14±4
7	2013 March 26	6378	14483	18.62	1.74	375±19	100±10	110±10	24±5
8	2013 April 24	6407	14484	18.62	1.74	314±18	93±10	90±10	34±6
9	2013 December 5	6632	14485	18.62	1.74	458±21	99±10	119±11	31±6
10	2013 December 28	6655	14486	18.61	1.74	339±18	134±12	138±12	45±7
11	2014 May 29	6807	14487	18.62	1.74	557±24	137±13	166±13	59±8
12	2014 June 10	6819	14488	18.62	1.74	520±23	163±12	150±12	55±7

[a] Julian Date − 2450000. [b] ACIS frame-time. [c]Background-subtracted source counts for events with energies in the 0.2–10 keV band.

TABLE 3
Log of Observations of Quasar SDSS 1004+4112

Epoch	Observation Date	JD[a] (days)	*Chandra* ObsID[b]	Time[c] (ks)	N_A[d] counts	N_B[d] counts	N_C[d] counts	N_D[d] counts
1	2010 March 8	5264	11546	5.96	53±7(16±4)	82±9(19±4)	66±8(20±4)	90±9(20±4)
2	2010 June 19	5367	11547	5.96	44±7(16±4)	44±7(15±4)	97±10(29±5)	84±9(14±4)
3	2010 September 23	5463	11548	5.96	51±7(13±4)	65±8(17±4)	66±8(22±5)	58±8(20±4)
4	2011 January 30	5592	11549	5.96	29±5(7±3)	36±6(14±4)	115±11(27±5)	85±9(28±5)
5	2013 January 27	6320	14495	24.74	192±14(60±8)	425±21(118±11)	360±19(94±10)	223±15(74±9)
6	2013 March 1	6353	14496	24.74	164±13(88±9)	414±20(139±12)	338±18(124±11)	184±14(83±9)
7	2013 October 5	6571	14497	24.13	179±13(87±9)	355±19(97±10)	356±19(114±11)	182±14(48±7)
8	2013 November 16	6613	14498	23.75	171±13(53±7)	358±19(98±10)	406±20(92±10)	250±16(83±9)
9	2014 April 29	6777	14499	23.32	139±12(65±8)	284±17(94±10)	245±16(82±9)	151±12(59±8)
10	2014 June 2	6811	14500	24.74	132±11(56±8)	422±21(132±11)	261±16(85±9)	138±12(45±7)

Note. — The ACIS-S frame-time for all observations is 3.1 s. [a] Julian Date − 2450000. [b] Observation ID. [c] Effective exposure time after applying filters. [d] Soft Band: 0.2–2 keV(hard band: 2–10 keV counts).

TABLE 4
PROPERTIES OF SAMPLE

Object	z_s	z_l	$L_{\rm Bol}/L_{\rm Edd}$	$\log(M_{\rm BH})$ $M_\odot$	$\log(R_{\rm E})$ cm	$\log(r_{\rm g})$ cm	R_E/v_e years	$10r_g/v_e$ months	v_e km/s	μ
RXJ1131	0.658	0.295	0.01-0.42	7.9-8.3	16.4	13.1-13.5	11.1	0.64-1.6	720	57
QJ0158	1.29	0.317	0.4	8.2	16.5	13.4	18.0	1.5	600	5
SDSS1004	1.73	0.68	0.05	8.6	16.4	13.8	9.4	2.9	785	70

NOTE. — $M_{\rm BH}$ and $R_{\rm E}$ are the black hole mass and Einstein radius ($\langle {\rm M} \rangle = 0.3 M_\odot$) with $r_{\rm g} = {\rm G}M_{\rm BH}/c^2$. R_E/v_e and r_g/v_e are the crossing times given the effective velocity v_e (see Mosquera & Kochanek 2011). The ACIS count-rates apply for of the combined images and represent average values based on available observations. μ is the total flux magnification of the background quasar. For the estimate of the Eddington ratios we assumed a 2–10 keV bolometric correction factor of $\kappa_{2-10{\rm keV}} \sim 30$.

TABLE 5
PROPERTIES OF SHIFTED Fe Kα LINE AND CONTINUUM IN RX J1131−1231

ObsID[a]	Image[b]	$E_{\rm Fe}$[c] keV	$\sigma_{\rm Fe}$[d] keV	$EW_{\rm Fe}$[e] keV	$N_{\rm Fe}$[f]	$N_{\rm cont}$[g]	Γ	$cstat$[h]	dof[h]	P[j]
4814	1	$3.96^{+0.13}_{-0.14}$	$0.15^{+0.13}_{-0.15}$	$1.66^{+0.46}_{-0.97}$	$4.5^{+3.3}_{-2.6}$	$7.3^{+1.5}_{-1.3}$	$1.48^{+0.19}_{-0.19}$	118.44	163	1
4814	2	$2.60^{+0.05}_{-0.05}$	< 0.12	$0.26^{+0.06}_{-0.09}$	$9.6^{+4.8}_{-4.8}$	$46.7^{+3.3}_{-3.1}$	$1.35^{+0.06}_{-0.06}$	491.61	491	1
6912	2	$3.46^{+0.09}_{-0.25}$	< 0.25	$0.35^{+0.25}_{-0.19}$	$4.6^{+5.0}_{-3.6}$	$47.0^{+5.7}_{-5.2}$	$1.76^{+0.12}_{-0.12}$	217.63	264	1
6913	1	$2.94^{+0.05}_{-0.27}$	$0.03^{+0.53}_{-0.03}$	$0.61^{+0.37}_{-0.36}$	$4.2^{+6.5}_{-3.2}$	$18.8^{+3.9}_{-3.4}$	$1.76^{+0.20}_{-0.20}$	116.63	152	1
6913	1	$3.81^{+0.20}_{-0.52}$	< 0.12	$1.11^{+0.73}_{-0.66}$	$4.7^{+6.0}_{-4.0}$	$18.8^{+3.9}_{-3.4}$	$1.76^{+0.20}_{-0.20}$	116.63	152	1
6913	4	$2.42^{+0.04}_{-0.04}$	< 0.15	$1.01^{+0.53}_{-0.48}$	$3.5^{+3.3}_{-2.2}$	$6.7^{+2.1}_{-1.7}$	$1.76^{+0.29}_{-0.29}$	52.03	77	0
6914	1	$4.59^{+0.44}_{-0.65}$	$0.45^{+1.13}_{-0.45}$	$2.52^{+1.62}_{-1.44}$	$12.4^{+9.3}_{-8.0}$	$23.6^{+4.2}_{-3.7}$	$1.66^{+0.17}_{-0.17}$	146.05	191	1
6914	2	$2.77^{+0.07}_{-0.06}$	$0.01^{+0.17}_{-0.01}$	$0.73^{+0.20}_{-0.31}$	$9.4^{+10.2}_{-4.4}$	$33.7^{+4.7}_{-4.2}$	$1.81^{+0.14}_{-0.14}$	175.40	234	0
6914	4	$3.63^{+0.68}_{-0.67}$	< 0.60	$1.00^{+1.00}_{-0.60}$	$2.1^{+2.7}_{-1.6}$	$9.1^{+2.5}_{-2.1}$	$1.83^{+0.27}_{-0.26}$	92.55	95	1
6915	1	$2.59^{+0.11}_{-0.15}$	$0.22^{+0.17}_{-0.16}$	$0.59^{+0.19}_{-0.17}$	$48.4^{+20.3}_{-18.9}$	$144.0^{+9.7}_{-9.2}$	$1.62^{+0.06}_{-0.06}$	445.59	476	0
6915	1	$4.35^{+0.10}_{-0.10}$	$0.08^{+0.09}_{-0.08}$	$0.31^{+0.18}_{-0.16}$	$11.1^{+9.5}_{-7.9}$	$144.0^{+9.7}_{-9.2}$	$1.62^{+0.06}_{-0.06}$	445.59	476	1
6915	2	$3.81^{+0.05}_{-0.03}$	< 0.07	$0.49^{+0.15}_{-0.38}$	$8.1^{+5.5}_{-4.3}$	$91.6^{+7.7}_{-7.3}$	$1.91^{+0.09}_{-0.09}$	333.73	343	0
6916	1	$2.28^{+0.10}_{-0.06}$	< 0.30	$0.16^{+0.07}_{-0.05}$	$15.8^{+10.8}_{-10.5}$	$147.0^{+9.8}_{-9.3}$	$1.58^{+0.06}_{-0.07}$	440.07	479	1
6916	1	$2.95^{+0.09}_{-0.07}$	< 0.50	$0.24^{+0.09}_{-0.07}$	$16.2^{+10.5}_{-10.5}$	$147.0^{+9.8}_{-9.3}$	$1.58^{+0.06}_{-0.07}$	440.07	479	1
7785	2	$2.69^{+0.03}_{-0.03}$	< 0.10	$0.48^{+0.14}_{-0.11}$	$12.8^{+7.0}_{-5.8}$	$72.0^{+6.7}_{-6.3}$	$1.86^{+0.10}_{-0.10}$	295.14	312	0
7785	2	$3.18^{+0.05}_{-0.28}$	< 0.10	$0.35^{+0.15}_{-0.21}$	$7.0^{+5.6}_{-4.4}$	$72.0^{+6.7}_{-6.3}$	$1.86^{+0.10}_{-0.10}$	295.14	312	1
7786	2	$3.42^{+0.15}_{-0.09}$	< 0.20	$0.35^{+0.15}_{-0.19}$	$9.7^{+9.7}_{-6.6}$	$89.0^{+7.1}_{-6.7}$	$1.70^{+0.08}_{-0.08}$	331.99	384	1
7787	1	$3.07^{+0.28}_{-0.23}$	$0.15^{+0.25}_{-0.15}$	$0.24^{+0.15}_{-0.16}$	$12.0^{+13.4}_{-11.4}$	$142.0^{+9.5}_{-9.0}$	$1.74^{+0.07}_{-0.07}$	421.39	439	1
7787	1	$4.20^{+0.04}_{-0.05}$	< 0.08	$0.32^{+0.20}_{-0.14}$	$9.4^{+6.8}_{-5.5}$	$142.0^{+9.5}_{-9.0}$	$1.74^{+0.07}_{-0.07}$	421.39	439	0
7788	1	$3.92^{+0.30}_{-0.23}$	< 1.10	$0.21^{+0.10}_{-0.11}$	$13.6^{+6.9}_{-5.4}$	$136.0^{+9.4}_{-9.0}$	$1.72^{+0.07}_{-0.07}$	362.37	423	1
7789	1	$2.49^{+0.08}_{-0.07}$	< 0.40	$0.17^{+0.07}_{-0.09}$	$11.4^{+8.6}_{-7.4}$	$146.0^{+9.7}_{-9.3}$	$1.82^{+0.07}_{-0.07}$	330.18	429	1
7789	2	$2.87^{+0.05}_{-0.04}$	< 0.11	$0.34^{+0.12}_{-0.15}$	$9.6^{+6.6}_{-5.3}$	$69.8^{+6.5}_{-6.1}$	$1.73^{+0.09}_{-0.09}$	300.51	339	0
7790	3	$2.42^{+0.20}_{-0.20}$	$0.24^{+0.21}_{-0.24}$	$1.04^{+0.36}_{-0.44}$	$13.0^{+9.6}_{-8.1}$	$21.7^{+3.7}_{-3.3}$	$1.69^{+0.16}_{-0.16}$	25.96	29	1
7791	2	$3.21^{+0.06}_{-0.05}$	< 0.10	$0.23^{+0.14}_{-0.13}$	$5.82^{+5.65}_{-4.42}$	$99.6^{+8.0}_{-7.5}$	$1.89^{+0.08}_{-0.08}$	294.67	340	1
7792	1	$2.55^{+0.07}_{-0.06}$	< 0.50	$0.20^{+0.10}_{-0.09}$	$11.3^{+9.1}_{-7.6}$	$145.0^{+10.0}_{-9.9}$	$1.92^{+0.08}_{-0.08}$	342.32	407	1
7792	2	$3.25^{+0.13}_{-0.12}$	$0.13^{+0.18}_{-0.13}$	$0.47^{+0.27}_{-0.21}$	$11.6^{+9.4}_{-7.6}$	$101.9^{+8.1}_{-7.7}$	$1.91^{+0.09}_{-0.08}$	333.74	363	1
7793	1	$3.75^{+0.05}_{-0.06}$	< 0.16	$0.22^{+0.12}_{-0.15}$	$6.7^{+6.3}_{-5.0}$	$122.9^{+8.9}_{-8.4}$	$1.75^{+0.07}_{-0.07}$	343.24	400	1
7793	2	$2.59^{+0.09}_{-0.07}$	$0.04^{+0.11}_{-0.04}$	$0.38^{+0.16}_{-0.22}$	$8.2^{+6.5}_{-6.0}$	$84.4^{+7.3}_{-6.9}$	$1.83^{+0.09}_{-0.09}$	312.71	346	1
7793	2	$4.97^{+0.09}_{-0.60}$	< 0.55	$0.46^{+0.31}_{-0.28}$	$4.9^{+13.4}_{-3.8}$	$84.4^{+7.3}_{-6.9}$	$1.83^{+0.09}_{-0.09}$	312.71	346	1
7793	3	$2.63^{+0.05}_{-0.05}$	< 0.12	$0.91^{+0.48}_{-0.54}$	$3.1^{+3.4}_{-2.2}$	$7.1^{+2.2}_{-1.8}$	$1.73^{+0.29}_{-0.29}$	85.62	82	1
7794	2	$4.37^{+0.07}_{-0.07}$	< 0.75	$0.41^{+0.23}_{-0.17}$	$8.0^{+17.9}_{-5.7}$	$114.1^{+8.4}_{-8.0}$	$1.79^{+0.08}_{-0.07}$	375.19	401	1
7794	3	$4.79^{+0.40}_{-0.39}$	< 0.14	$0.65^{+0.51}_{-0.40}$	$3.0^{+3.9}_{-2.5}$	$38.0^{+5.0}_{-4.6}$	$1.89^{+0.14}_{-0.13}$	166.94	221	1
9180	1	$2.81^{+0.07}_{-0.10}$	$0.05^{+0.43}_{-0.05}$	$0.11^{+0.04}_{-0.06}$	$5.8^{+7.5}_{-4.2}$	$101.6^{+4.5}_{-4.4}$	$1.62^{+0.04}_{-0.04}$	558.90	596	1
9180	3	$3.53^{+0.06}_{-0.07}$	< 0.17	$0.23^{+0.12}_{-0.14}$	$2.0^{+1.9}_{-1.5}$	$33.7^{+2.6}_{-2.5}$	$1.77^{+0.08}_{-0.08}$	368.30	385	1
9181	1	$2.35^{+0.10}_{-0.10}$	$0.15^{+0.11}_{-0.10}$	$0.20^{+0.06}_{-0.07}$	$18.2^{+10.7}_{-9.5}$	$142.1^{+5.4}_{-5.2}$	$1.65^{+0.04}_{-0.04}$	632.52	638	0
9181	1	$2.80^{+0.05}_{-0.05}$	< 0.12	$0.11^{+0.04}_{-0.06}$	$7.2^{+4.3}_{-4.3}$	$142.1^{+5.4}_{-5.2}$	$1.65^{+0.04}_{-0.04}$	632.52	638	1
9181	4	$3.70^{+0.05}_{-0.30}$	< 0.12	$0.59^{+0.36}_{-0.36}$	$1.5^{+1.3}_{-1.0}$	$12.0^{+1.6}_{-1.4}$	$1.84^{+0.13}_{-0.13}$	192.77	227	1

NOTE. — [a] *Chandra* Observation ID, [b] Image numbers 1, 2, 3, and 4 correspond to images A, B, C, and D of RX J1131−1231, [c] Observed-frame energy of the shifted Fe line, [d] Observed-frame energy width of the shifted Fe line, [e] Rest-frame equivalent width of the shifted Fe line, [f] Flux of the shifted Fe line in units of $\times\ 10^{-6}$ photons cm^{-2} s^{-1}, [g] Flux density of the continuum in units of $\times\ 10^{-5}$ photons keV^{-1} cm^{-2} s^{-1} at 1 keV, [h] Cash statistic, [i] degrees of freedom, [j] P values of 0 and 1 correspond to confidence detection levels of the shifted Fe line of $> 99\%$ and $> 90\%$ respectively.

TABLE 5
(CONTINUED)

ObsID[a]	Image	$E_{\rm Fe}$ keV	$\sigma_{\rm Fe}$ keV	$EW_{\rm Fe}$ keV	$N_{\rm Fe}$ [c]	$N_{\rm cont}$ [d]	Γ	cstat	dof	P
9237	2	$3.16^{+0.06}_{-0.05}$	< 0.13	$0.12^{+0.07}_{-0.06}$	$4.0^{+3.5}_{-2.8}$	$90.2^{+4.2}_{-4.0}$	$1.65^{+0.04}_{-0.04}$	560.80	584	1
9237	3	$3.84^{+0.06}_{-0.05}$	$0.05^{+0.08}_{-0.05}$	$0.59^{+0.19}_{-0.22}$	$3.8^{+2.4}_{-1.9}$	$30.7^{+2.5}_{-2.4}$	$1.81^{+0.08}_{-0.08}$	322.8	353	0
9237	4	$3.46^{+0.15}_{-0.28}$	$0.19^{+0.32}_{-0.08}$	$1.61^{+0.59}_{-0.60}$	$3.3^{+2.1}_{-1.7}$	$6.8^{+1.2}_{-1.1}$	$1.7^{+0.18}_{-0.17}$	183.75	195	0
9238	3	$2.72^{+0.10}_{-0.10}$	$0.13^{+0.13}_{-0.10}$	$0.72^{+0.27}_{-0.22}$	$5.8^{+3.7}_{-3.0}$	$21.4^{+2.2}_{-2.0}$	$1.85^{+0.10}_{-0.10}$	253.35	316	0
9238	3	$3.80^{+0.10}_{-0.09}$	$0.10^{+0.11}_{-0.10}$	$0.65^{+0.26}_{-0.29}$	$2.8^{+2.2}_{-1.8}$	$21.4^{+2.2}_{-2.0}$	$1.85^{+0.10}_{-0.10}$	253.35	316	0
9239	2	$2.41^{+0.07}_{-0.29}$	$0.05^{+0.28}_{-0.05}$	$0.13^{+0.07}_{-0.05}$	$4.9^{+8.0}_{-3.6}$	$63.5^{+3.5}_{-3.4}$	$1.65^{+0.05}_{-0.05}$	503.17	514	1
9240	2	$3.06^{+0.05}_{-0.29}$	< 0.10	$0.22^{+0.08}_{-0.07}$	$5.0^{+2.9}_{-2.9}$	$62.4^{+3.6}_{-3.6}$	$1.72^{+0.06}_{-0.06}$	498.60	495	1
9240	2	$3.96^{+0.17}_{-0.14}$	$0.20^{+0.24}_{-0.11}$	$0.55^{+0.24}_{-0.22}$	$8.1^{+7.5}_{-4.5}$	$62.4^{+3.6}_{-3.6}$	$1.72^{+0.06}_{-0.06}$	498.60	495	1
9240	4	$3.34^{+0.04}_{-0.04}$	< 0.06	$0.46^{+0.19}_{-0.18}$	$1.8^{+1.5}_{-1.1}$	$12.4^{+1.6}_{-1.5}$	$1.73^{+0.12}_{-0.12}$	228.56	260	1
11540	2	$3.27^{+0.04}_{-0.05}$	< 0.10	$0.09^{+0.04}_{-0.03}$	$3.2^{+2.2}_{-2.0}$	$91.4^{+3.1}_{-3.0}$	$1.63^{+0.03}_{-0.03}$	678.26	681	1
11540	2	$4.28^{+0.05}_{-0.05}$	< 0.12	$0.16^{+0.23}_{-0.12}$	$3.4^{+2.0}_{-2.0}$	$91.4^{+3.1}_{-3.0}$	$1.63^{+0.03}_{-0.03}$	678.26	681	1
11540	3	$3.93^{+0.08}_{-0.16}$	$0.05^{+0.14}_{-0.05}$	$0.21^{+0.10}_{-0.15}$	$2.2^{+2.1}_{-1.6}$	$35.7^{+2.3}_{-2.1}$	$1.61^{+0.06}_{-0.06}$	411.79	496	1
11542	1	$2.36^{+0.05}_{-0.05}$	$0.13^{+0.06}_{-0.05}$	$0.22^{+0.04}_{-0.04}$	$3.0^{+9.9}_{-9.0}$	$149.7^{+4.1}_{-4.1}$	$1.39^{+0.02}_{-0.02}$	963.88	822	0
11542	1	$2.94^{+0.09}_{-0.09}$	$0.11^{+0.20}_{-0.07}$	$0.22^{+0.05}_{-0.04}$	$1.2^{+9.7}_{-6.3}$	$149.7^{+4.1}_{-4.1}$	$1.39^{+0.02}_{-0.02}$	963.88	822	0
11542	2	$3.18^{+0.03}_{-0.05}$	< 0.10	$0.13^{+0.06}_{-0.05}$	$3.6^{+2.1}_{-2.1}$	$62.1^{+2.6}_{-2.6}$	$1.58^{+0.04}_{-0.04}$	633.02	641	1
11543	1	$2.31^{+0.04}_{-0.04}$	< 0.13	$0.06^{+0.02}_{-0.03}$	$8.0^{+4.6}_{-4.6}$	$151.2^{+4.4}_{-4.4}$	$1.44^{+0.03}_{-0.03}$	233.51	184	1
11543	1	$2.62^{+0.04}_{-0.04}$	< 0.07	$0.08^{+0.02}_{-0.02}$	$8.7^{+4.2}_{-4.1}$	$151.2^{+4.4}_{-4.4}$	$1.44^{+0.03}_{-0.03}$	233.51	184	0
11543	3	$2.62^{+0.05}_{-0.06}$	< 0.10	$0.17^{+0.11}_{-0.08}$	$2.4^{+2.0}_{-1.7}$	$30.6^{+2.3}_{-2.2}$	$1.75^{+0.07}_{-0.07}$	354.98	408	1
11543	3	$4.30^{+0.04}_{-0.05}$	< 0.10	$0.34^{+0.14}_{-0.13}$	$2.0^{+1.6}_{-1.2}$	$30.6^{+2.3}_{-2.2}$	$1.75^{+0.07}_{-0.07}$	354.98	408	1
11544	3	$3.83^{+0.05}_{-0.05}$	< 0.28	$0.25^{+0.13}_{-0.12}$	$2.3^{+1.7}_{-1.4}$	$35.6^{+2.5}_{-2.4}$	$1.71^{+0.07}_{-0.07}$	104.89	130	1
11545	3	$2.96^{+0.06}_{-0.06}$	< 0.10	$0.28^{+0.12}_{-0.13}$	$2.1^{+1.7}_{-1.3}$	$20.2^{+2.0}_{-1.8}$	$1.75^{+0.09}_{-0.09}$	319.40	348	0
11545	3	$4.44^{+0.13}_{-0.14}$	$0.20^{+0.13}_{-0.14}$	$1.30^{+0.52}_{-0.46}$	$4.8^{+2.8}_{-2.3}$	$20.2^{+2.0}_{-1.8}$	$1.75^{+0.09}_{-0.09}$	319.40	348	0
12833	1	$3.97^{+0.04}_{-0.05}$	< 0.2	$0.21^{+0.07}_{-0.06}$	$6.4^{+3.6}_{-3.2}$	$121.5^{+5.5}_{-5.3}$	$1.69^{+0.04}_{-0.04}$	492.66	577	0
12833	2	$4.22^{+0.20}_{-0.33}$	$0.13^{+0.23}_{-0.13}$	$0.25^{+0.16}_{-0.13}$	$4.9^{+5.0}_{-4.0}$	$108.0^{+5.2}_{-5.0}$	$1.82^{+0.04}_{-0.04}$	497.50	542	1
12833	3	$4.84^{+0.12}_{-0.16}$	$0.1^{+0.24}_{-0.10}$	$0.74^{+0.33}_{-0.34}$	$4.0^{+3.8}_{-2.7}$	$40.7^{+3.8}_{-3.6}$	$1.84^{+0.09}_{-0.09}$	337.96	346	1
12834	2	$3.84^{+0.07}_{-0.08}$	$0.06^{+0.10}_{-0.06}$	$0.22^{+0.11}_{-0.11}$	$4.5^{+3.7}_{-3.0}$	$78.5^{+4.5}_{-4.3}$	$1.69^{+0.05}_{-0.05}$	496.96	522	1
12834	4	$4.42^{+0.05}_{-0.06}$	< 0.15	$0.66^{+0.46}_{-0.41}$	$1.0^{+1.2}_{-0.8}$	$9.0^{+1.6}_{-1.4}$	$1.82^{+0.16}_{-0.16}$	160.98	184	1
13962	1	$2.62^{+0.21}_{-0.28}$	< 0.80	$0.13^{+0.10}_{-0.10}$	$3.6^{+4.0}_{-3.3}$	$71.5^{+4.9}_{-4.6}$	$1.81^{+0.07}_{-0.07}$	423.80	454	1
13962	1	$3.91^{+0.30}_{-0.27}$	$0.38^{+0.28}_{-0.21}$	$0.80^{+0.43}_{-0.31}$	$11.5^{+8.5}_{-6.8}$	$71.5^{+4.9}_{-4.6}$	$1.81^{+0.07}_{-0.07}$	423.80	454	0
13962	3	$3.83^{+0.23}_{-0.18}$	$0.25^{+0.30}_{-0.20}$	$1.09^{+0.53}_{-0.28}$	$5.2^{+3.8}_{-2.9}$	$29.1^{+3.1}_{-2.8}$	$1.95^{+0.11}_{-0.11}$	267.15	324	0
13962	4	$3.90^{+0.07}_{-0.07}$	< 0.12	$0.38^{+0.20}_{-0.22}$	$1.4^{+1.5}_{-1.1}$	$20.1^{+2.4}_{-2.2}$	$1.87^{+0.11}_{-0.11}$	241.22	278	1
13963	1	$2.39^{+0.07}_{-0.08}$	$0.03^{+0.08}_{-0.03}$	$0.21^{+0.11}_{-0.11}$	$3.8^{+3.2}_{-2.9}$	$33.2^{+3.3}_{-3.2}$	$1.73^{+0.10}_{-0.10}$	401.43	403	1
13963	1	$3.29^{+0.07}_{-0.06}$	< 0.30	$0.22^{+0.07}_{-0.10}$	$2.8^{+2.4}_{-1.9}$	$33.2^{+3.3}_{-3.2}$	$1.73^{+0.10}_{-0.10}$	401.43	403	1
13963	2	$2.30^{+0.09}_{-0.09}$	$0.08^{+0.10}_{-0.08}$	$0.19^{+0.10}_{-0.11}$	$7.3^{+5.8}_{-4.6}$	$57.8^{+3.9}_{-3.7}$	$1.65^{+0.06}_{-0.06}$	463.75	506	1
13963	2	$3.92^{+0.07}_{-0.06}$	$0.02^{+0.10}_{-0.02}$	$0.19^{+0.01}_{-0.01}$	$3.1^{+2.8}_{-2.2}$	$57.8^{+3.9}_{-3.7}$	$1.65^{+0.06}_{-0.06}$	463.75	506	1
13963	3	$2.42^{+0.10}_{-0.30}$	$0.04^{+0.40}_{-0.04}$	$0.23^{+0.15}_{-0.17}$	$2.2^{+5.2}_{-1.8}$	$15.8^{+2.1}_{-1.9}$	$1.68^{+0.12}_{-0.12}$	240.66	294	1
14507	1	$3.82^{+0.27}_{-0.27}$	< 0.14	$0.39^{+0.18}_{-0.19}$	$3.3^{+3.0}_{-2.2}$	$26.4^{+3.6}_{-3.2}$	$1.59^{+0.12}_{-0.12}$	268.03	282	1
14507	2	$3.60^{+0.05}_{-0.05}$	$0.05^{+0.08}_{-0.05}$	$0.54^{+0.20}_{-0.15}$	$6.7^{+4.2}_{-3.3}$	$42.9^{+4.3}_{-4.0}$	$1.70^{+0.09}_{-0.09}$	309.99	361	0
14507	3	$4.30^{+0.11}_{-0.29}$	$0.05^{+0.33}_{-0.05}$	$0.35^{+0.04}_{-0.03}$	$2.3^{+3.4}_{-1.7}$	$14.5^{+2.7}_{-2.3}$	$1.77^{+0.17}_{-0.16}$	150.66	198	1
14508	3	$4.24^{+0.23}_{-0.22}$	$0.30^{+1.00}_{-0.30}$	$1.59^{+0.80}_{-0.77}$	$6.2^{+4.1}_{-3.5}$	$19.4^{+3.0}_{-2.7}$	$1.74^{+0.14}_{-0.14}$	195.38	249	1
14510	4	$4.63^{+0.22}_{-0.21}$	$0.30^{+0.50}_{-0.10}$	$2.43^{+1.04}_{-1.11}$	$6.0^{+3.8}_{-3.2}$	$20.1^{+3.3}_{-2.9}$	$1.91^{+0.15}_{-0.15}$	46.62	61	1

TABLE 6
PROPERTIES OF SHIFTED Fe Kα LINE AND CONTINUUM IN QJ 0158−4325

ObsID[a]	Image	$E_{\rm Fe}$ keV	$\sigma_{\rm Fe}$ keV	$EW_{\rm Fe}$ keV	$N_{\rm Fe}$ [c]	$N_{\rm cont}$ [d]	Γ	cstat	dof	P
14487	2	$3.63^{+0.04}_{-0.04}$	$0.01^{+0.20}_{-0.01}$	$1.14^{+0.70}_{-0.62}$	$2.1^{+2.4}_{-1.6}$	$2.2^{+0.4}_{-0.3}$	$1.94^{+0.23}_{-0.23}$	101.83	111	1
14486	1	$3.41^{+0.21}_{-0.15}$	$0.39^{+0.60}_{-0.39}$	$2.25^{+0.98}_{-0.73}$	$7.1^{+4.3}_{-3.4}$	$4.8^{+0.5}_{-0.5}$	$1.92^{+0.16}_{-0.15}$	157.29	170	0
14485	1	$2.93^{+0.06}_{-0.06}$	$0.14^{+0.14}_{-0.14}$	$1.01^{+0.36}_{-0.40}$	$6.8^{+4.6}_{-3.7}$	$6.7^{+0.6}_{-0.6}$	$2.19^{+0.17}_{-0.16}$	166.84	191	0
14485	1	$4.37^{+0.57}_{-0.35}$	$1.10^{+1.50}_{-0.60}$	$3.86^{+1.61}_{-1.51}$	$10.3^{+6.6}_{-5.8}$	$6.7^{+0.6}_{-0.6}$	$2.19^{+0.17}_{-0.16}$	166.84	191	0
14484	1	$2.86^{+0.06}_{-0.06}$	< 1.9	$0.63^{+0.61}_{-0.49}$	$3.0^{+2.6}_{-1.9}$	$3.6^{+0.4}_{-0.3}$	$1.97^{+0.15}_{-0.15}$	152.69	168	1
14484	2	$2.83^{+0.13}_{-0.26}$	$0.3^{+1.1}_{-0.3}$	$2.21^{+1.24}_{-1.06}$	$4.2^{+3.6}_{-2.7}$	$1.3^{+0.3}_{-0.2}$	$1.92^{+0.30}_{-0.29}$	68.33	80	1
11561	1	$2.27^{+0.39}_{-0.35}$	$0.4^{+0.8}_{-0.4}$	$2.19^{+1.12}_{-0.96}$	$14.8^{+11.9}_{-9.4}$	$4.2^{+0.7}_{-0.6}$	$2.26^{+0.30}_{-0.28}$	55.67	81	1
11561	2	$2.84^{+0.31}_{-0.31}$	$0.5^{+1.3}_{-0.4}$	$4.41^{+2.63}_{-2.36}$	$10.5^{+10.9}_{-8.2}$	$2.2^{+0.6}_{-0.5}$	$2.13^{+0.45}_{-0.50}$	30.53	41	1
11560	1	$1.59^{+0.06}_{-0.06}$	$0.12^{+0.30}_{-0.12}$	$0.58^{+0.26}_{-0.24}$	$11.7^{+8.6}_{-7.0}$	$4.7^{+0.8}_{-0.7}$	$1.81^{+0.23}_{-0.23}$	106.62	105	1
11557	1	$1.73^{+0.04}_{-0.03}$	$0.01^{+0.13}_{-0.01}$	$0.55^{+0.28}_{-0.25}$	$10.4^{+8.7}_{-6.6}$	$5.5^{+0.9}_{-0.8}$	$1.94^{+0.26}_{-0.25}$	76.04	88	1

NOTE. — [a] *Chandra* Observation ID, [b]Image numbers 1 and 2 correspond to images A and B of QJ 0158−4325, [c]Observed-frame energy of the shifted Fe line, [d] Observed-frame energy width of the shifted Fe line, [e]Rest-frame equivalent width of the shifted Fe line, [f]Flux of the shifted Fe line in units of $\times\ 10^{-6}$ photons cm^{-2} s^{-1}, [g]Flux density of the continuum in units of $\times\ 10^{-5}$ photons keV^{-1} cm^{-2} s^{-1} at 1 keV, [h] Cash statistic, [i]degrees of freedom, [j]P values of 0 and 1 correspond to confidence detection levels of the shifted Fe line of $> 99\%$ and $> 90\%$ respectively.

TABLE 7
PROPERTIES OF SHIFTED FE Kα LINE AND CONTINUUM IN SDSS 1004+4112

ObsID[a]	Image	$E_{\rm Fe}$ keV	$\sigma_{\rm Fe}$ keV	$EW_{\rm Fe}$ keV	$N_{\rm Fe}$ [c]	$N_{\rm cont}$ [d]	Γ	cstat	dof	P
11549	4	$1.18^{+0.04}_{-0.03}$	<0.1	$0.60^{+0.27}_{-0.25}$	$3.6^{+2.8}_{-2.2}$	$10.8^{+5.6}_{-3.9}$	$1.59^{+0.28}_{-0.29}$	57.68	80	0
14495	2	$2.12^{+0.05}_{-0.21}$	<0.16	$0.61^{+0.23}_{-0.31}$	$1.8^{+1.4}_{-1.1}$	$21.0^{+2.9}_{-3.5}$	$1.89^{+0.13}_{-0.13}$	152.36	185	0
14495	4	$2.33^{+0.14}_{-0.13}$	$0.30^{+0.13}_{-0.10}$	$4.36^{+1.30}_{-1.08}$	$4.4^{+1.8}_{-1.7}$	$15.3^{+4.7}_{-3.6}$	$2.17^{+0.23}_{-0.21}$	124.95	150	0
14496	2	$3.10^{+0.06}_{-0.07}$	<0.12	$0.74^{+0.34}_{-0.34}$	$1.2^{+1.0}_{-0.8}$	$19.4^{+3.9}_{-3.3}$	$1.79^{+0.13}_{-0.13}$	185.30	200	1
14496	3	$2.36^{+0.07}_{-0.07}$	<0.20	$1.71^{+0.60}_{-0.56}$	$2.8^{+1.5}_{-1.5}$	$16.5^{+5.1}_{-4.0}$	$1.93^{+0.21}_{-0.19}$	159.62	196	0
14498	1	$1.80^{+0.05}_{-0.36}$	<0.37	$0.58^{+0.26}_{-0.24}$	$1.0^{+0.7}_{-0.6}$	$8.3^{+3.0}_{-2.2}$	$1.81^{+0.21}_{-0.21}$	94.73	124	0
14498	1	$2.23^{+0.05}_{-0.08}$	<0.11	$1.02^{+0.51}_{-0.50}$	$1.2^{+1.0}_{-0.8}$	$8.3^{+3.0}_{-2.2}$	$1.81^{+0.21}_{-0.21}$	94.73	124	0
14500	2	$1.81^{+0.05}_{-0.04}$	<0.10	$0.30^{+0.12}_{-0.12}$	$1.3^{+1.0}_{-0.8}$	$23.2^{+4.8}_{-4.0}$	$1.84^{+0.13}_{-0.13}$	178.21	204	1

NOTE. — [a] *Chandra* Observation ID, [b]Image numbers 1, 2, 3, and 4 correspond to images A, B, C, and D of SDSS 1004+4112, [c]Observed-frame energy of the shifted Fe line, [d] Observed-frame energy width of the shifted Fe line, [e]Rest-frame equivalent width of the shifted Fe line, [f]Flux of the shifted Fe line in units of $\times$ 10^{-6} photons cm^{-2} s^{-1}, [g]Flux density of the continuum in units of $\times$ 10^{-5} photons keV^{-1} cm^{-2} s^{-1} at 1 keV, [h] Cash statistic, [i]degrees of freedom, [j]P values of 0 and 1 correspond to confidence detection levels of the shifted Fe line of $>$ 99% and $>$ 90% respectively.

TABLE 8
Correlation Results of RX J1131−1231.

TEST	QUANTITY I	QUANTITY II	$N_{\rm sample}$ [a]	STATISTIC	CHANCE PROBABILITY
Spearman's (ρ)	$E_{\rm min}$ [b]	$E_{\rm max}$ [b]	9	0.78	0.015
Kendalls's (τ)	$E_{\rm min}$ [b]	$E_{\rm max}$ [b]	9	0.61	0.022
Spearman's (ρ)	$E_{\rm min}$ [c]	$E_{\rm max}$ [c]	17	0.52	0.032
Kendalls's (τ)	$E_{\rm min}$ [c]	$E_{\rm max}$ [c]	17	0.39	0.031
Spearman's (ρ)	$EW_{\rm Fe}$	g	78	0.42	1.6×10^{-4}
Kendalls's (τ)	$EW_{\rm Fe}$	g	78	0.28	2.4×10^{-4}
Spearman's (ρ)	$N_{\rm Fe}$	$N_{\rm cont}$	78	0.69	4.4×10^{-12}
Kendalls's (τ)	$N_{\rm Fe}$	$N_{\rm cont}$	78	0.50	$< 1 \times 10^{-12}$

Note. — Spearman's (ρ) and Kendalls's (τ) rank correlations of two sample populations labelled QUANTITY I and QUANTITY II. [a] The number of elements in the sample. [b] Rest-frame energies of the shifted double Fe lines in image A detected at the $> 90\%$ confidence level. [c] Rest-frame energies of the shifted double Fe lines in all images detected at the $> 90\%$ confidence level.

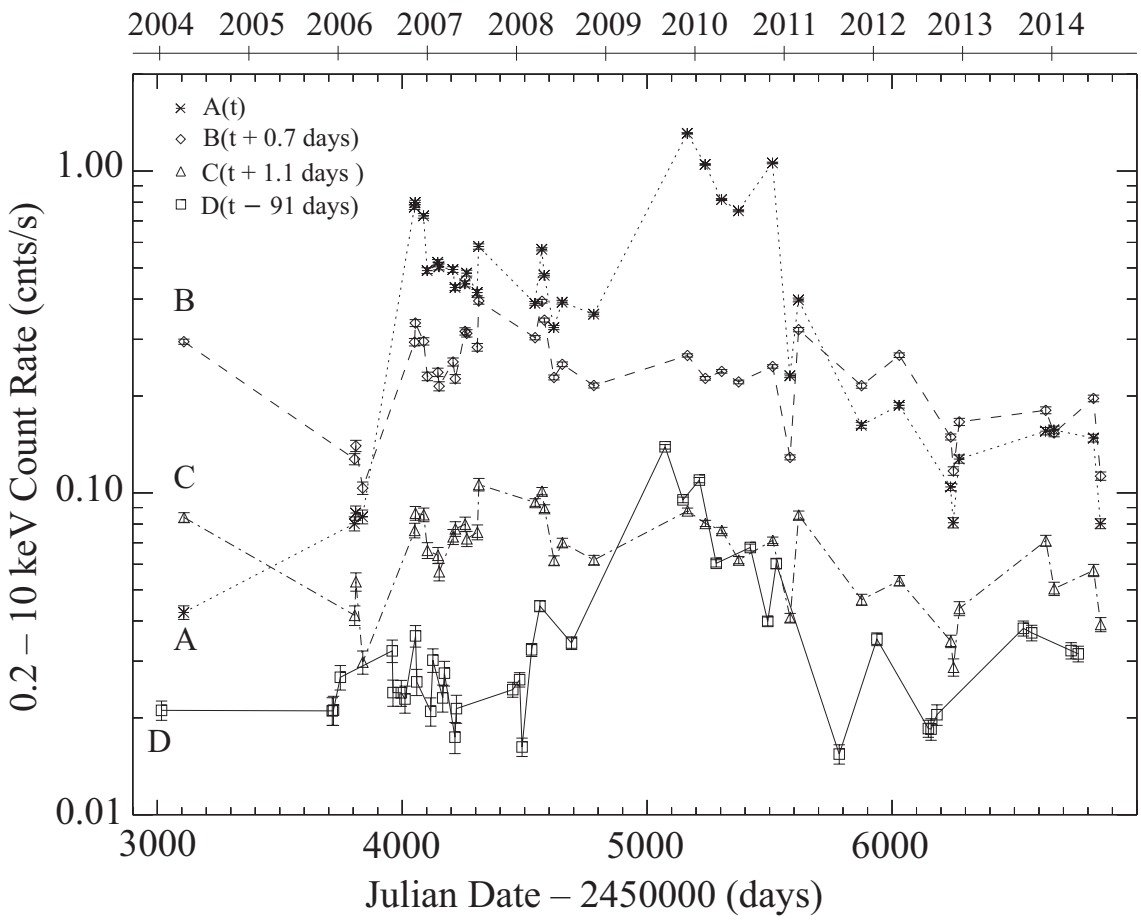

FIG. 1.— The total (0.2–10 keV) light-curves of images A, B, C and D of RX J1131−1231 shifted by the time delays estimated by Tewes et al. (2012). The total counts for images A and B have been corrected for pile-up effects while pile-up is unimportant for images C and D. The new X-ray data begin after epoch 29 (February 2011, JD − 2450000 = 5618).

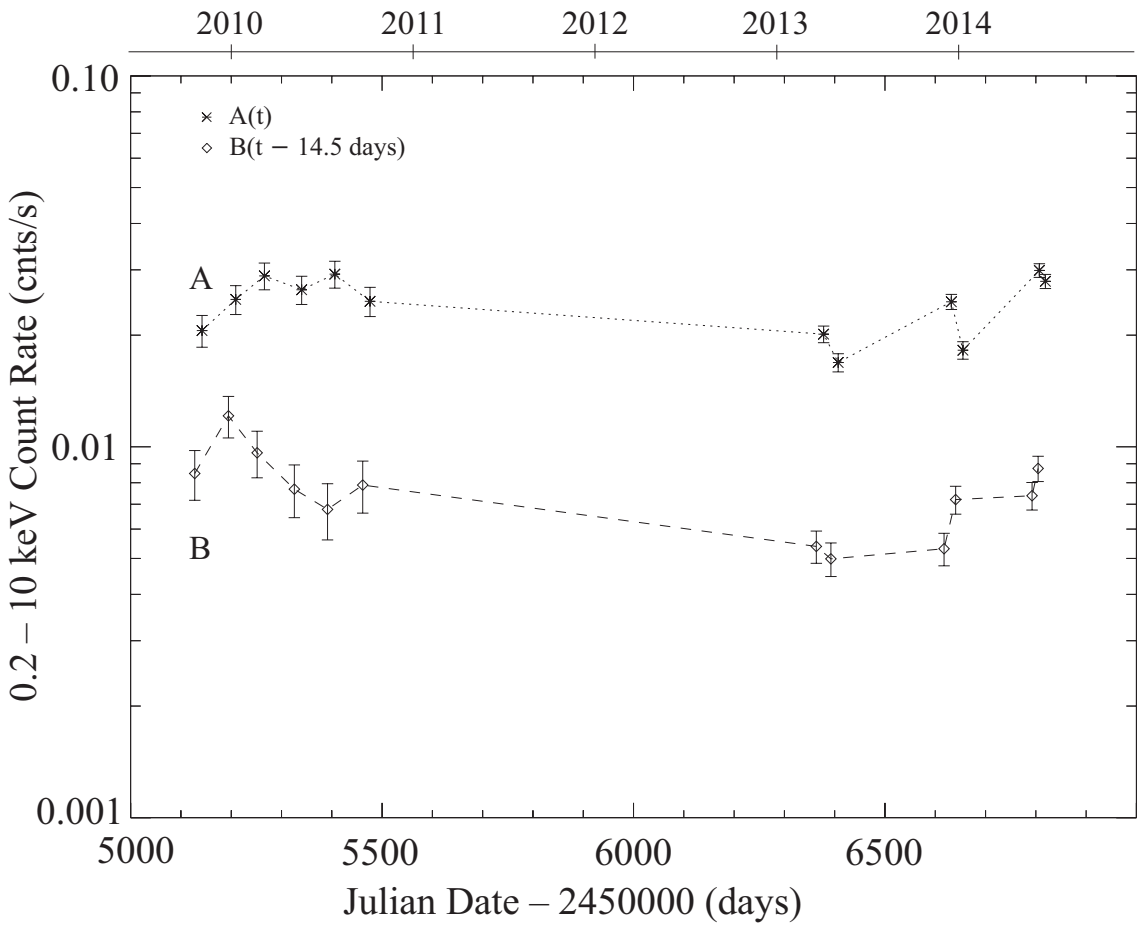

FIG. 2.— The total (0.2–10 keV) light-curves of images A and B of QJ 0158−4325 shifted by the time delay of $\Delta t_{A-B} = -14.5$ days estimated by Faure et al. (2009). The new X-ray data begin after epoch 6 (October 2010, JD − 2450000 = 5476).

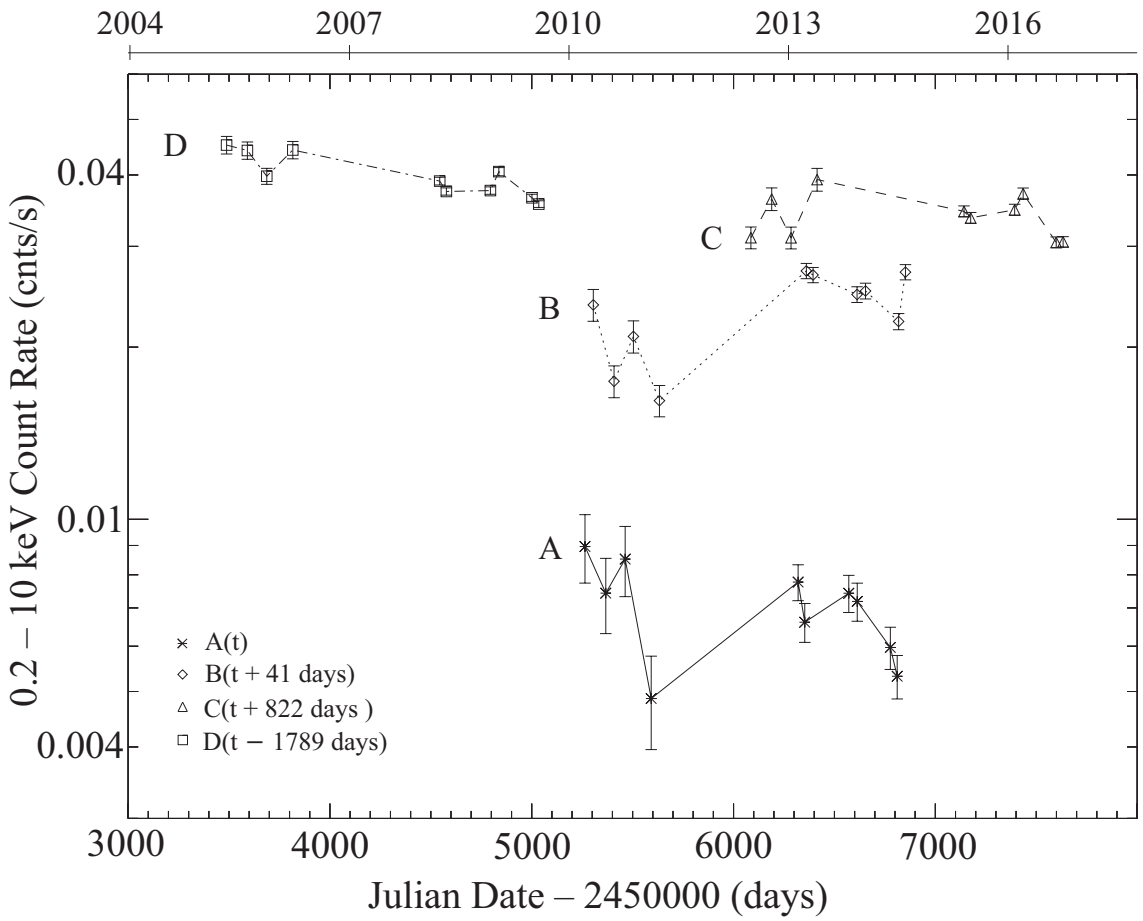

FIG. 3.— The total (0.2–10 keV) light-curves of images A, B, C, and D of SDSS 1004+4112 shifted by the time delays estimated by Fohlmeister et al. (2008, 2016). We have added offsets of 0.01 cnts s^{-1}, 0.02 cnts s^{-1}, and 0.03 cnts s^{-1} to the light-curves of the images B, C, and D, respectively, for clarity. The new X-ray data begin after epoch 5 (March 2013, JD − 2450000 = 6353).

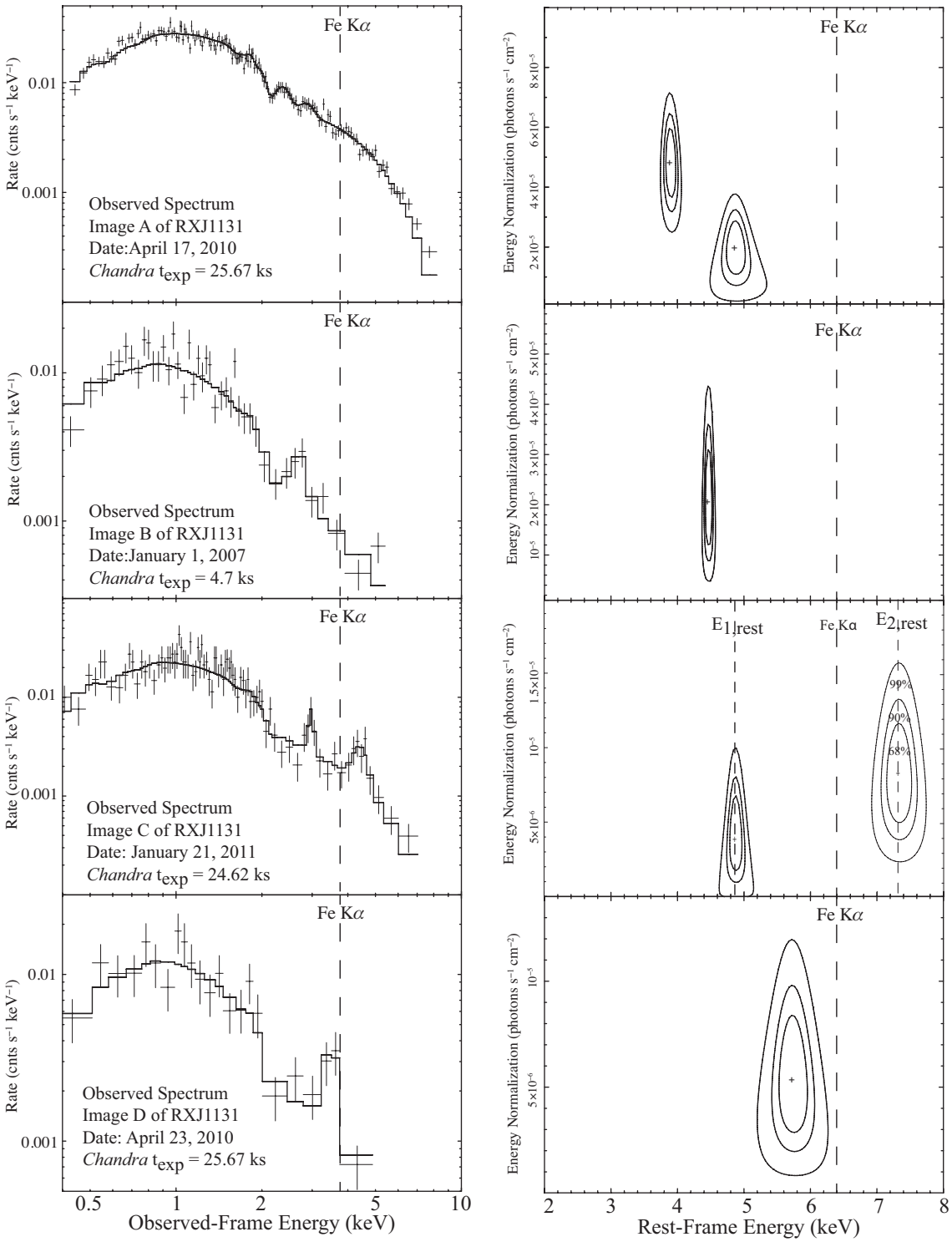

FIG. 4.— (left) Spectra of images A,B,C, and D of RXJ1131 at 4 different epochs showing the shifted iron lines. The best-fit model is comprised of a power law, one or two Gaussian lines, plus Galactic and intrinsic absorption. (right) The 68%, 90%, and 99% χ^2 confidence contours for the line energies and flux normalizations.

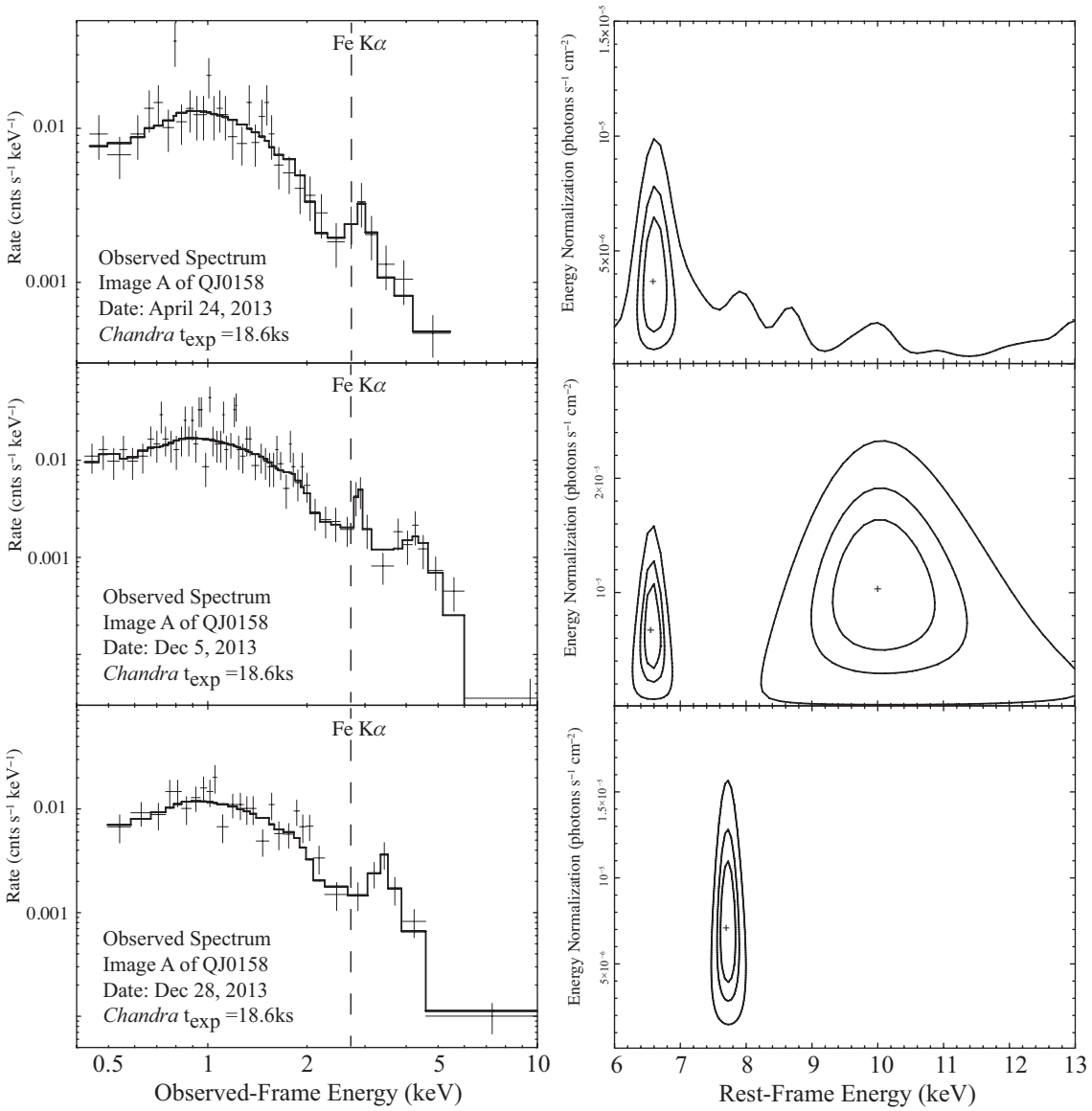

FIG. 5.— (left) Spectra of image A of QJ0158 at 3 different epochs showing the shifted iron lines. The best-fit models are comprised of a power law, and one or two Gaussian lines, plus Galactic and intrinsic absorption. (right) The 68%, 90%, and 99% χ^2 confidence contours for the line energies and flux normalizations.

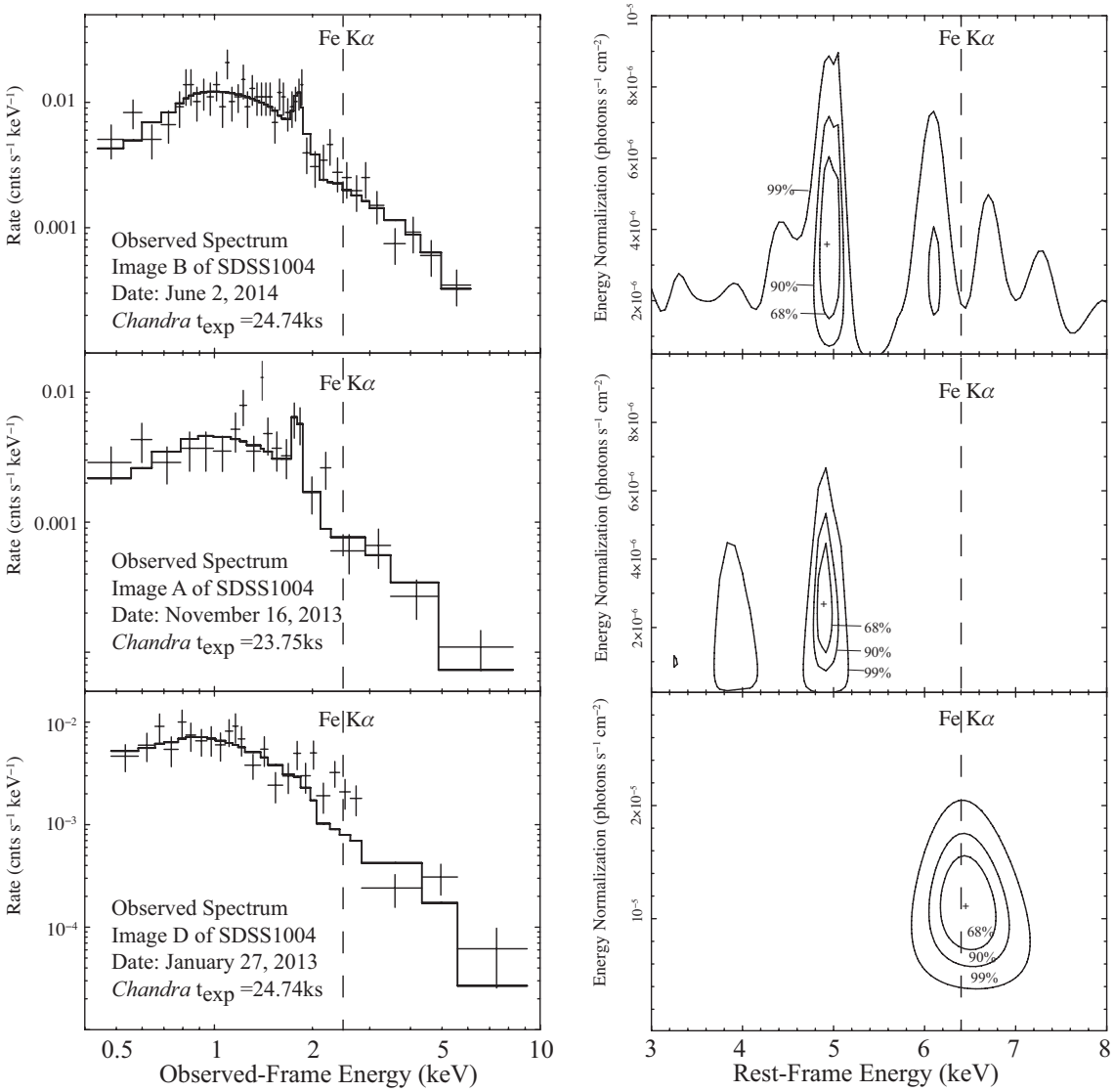

FIG. 6.— (left) Spectra of images B, A, and D of SDSS1004 at 3 different epochs showing shifted iron lines. The best-fit models are comprised of a power law, and a Gaussian line, plus Galactic and intrinsic absorption. The model for image D does not include the Gaussian line to better show the residual line emission near the instrumental edge at $\sim$ 2 keV. (right) The 68%, 90%, and 99% χ^2 confidence contours for the line energies and flux normalizations.

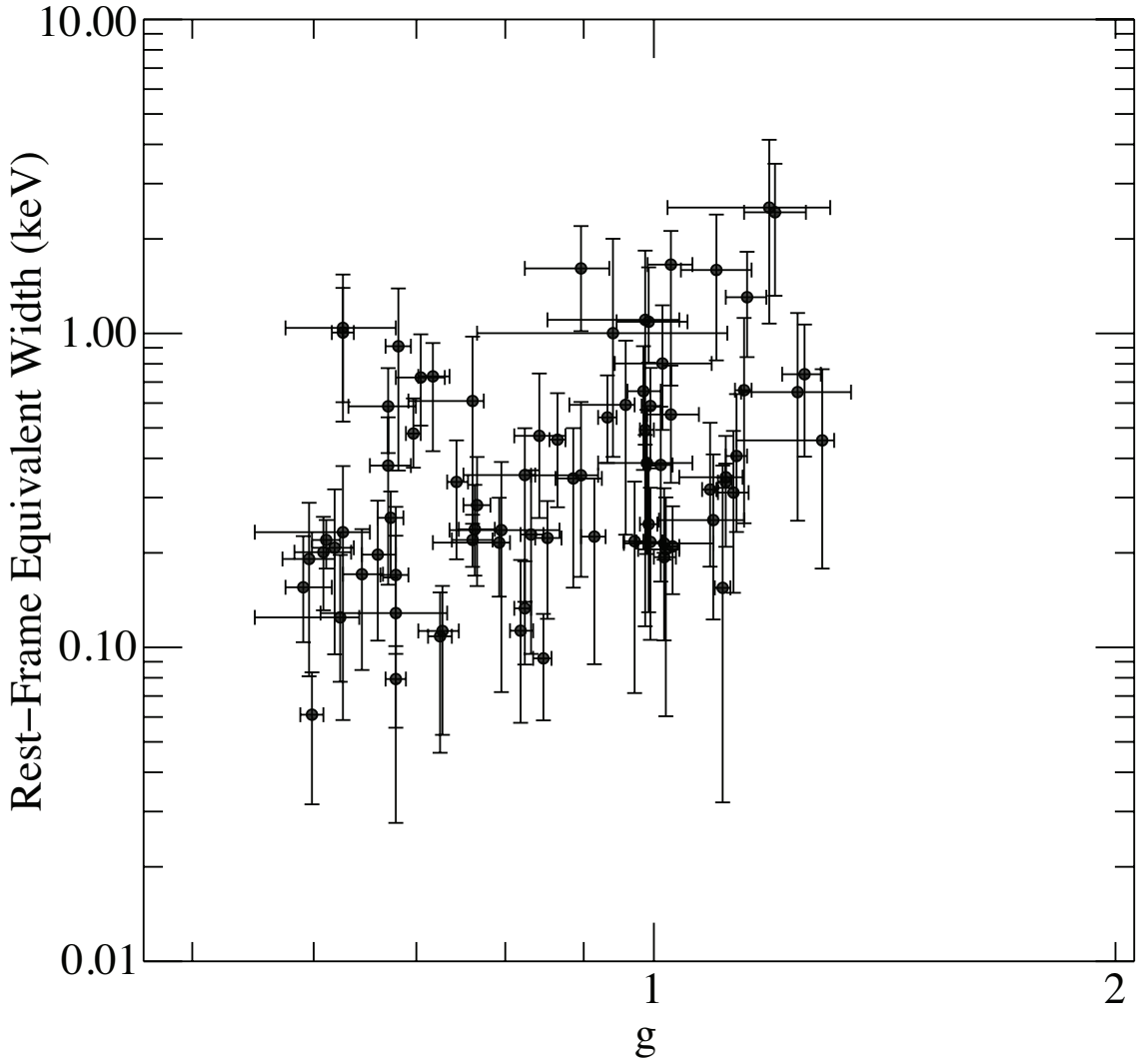

FIG. 7.— The Fe line equivalent width as a function of the generalized Doppler shift parameter g for all images of RXJ1131. Only cases where the Fe line is detected at $> 90\%$ confidence are shown.

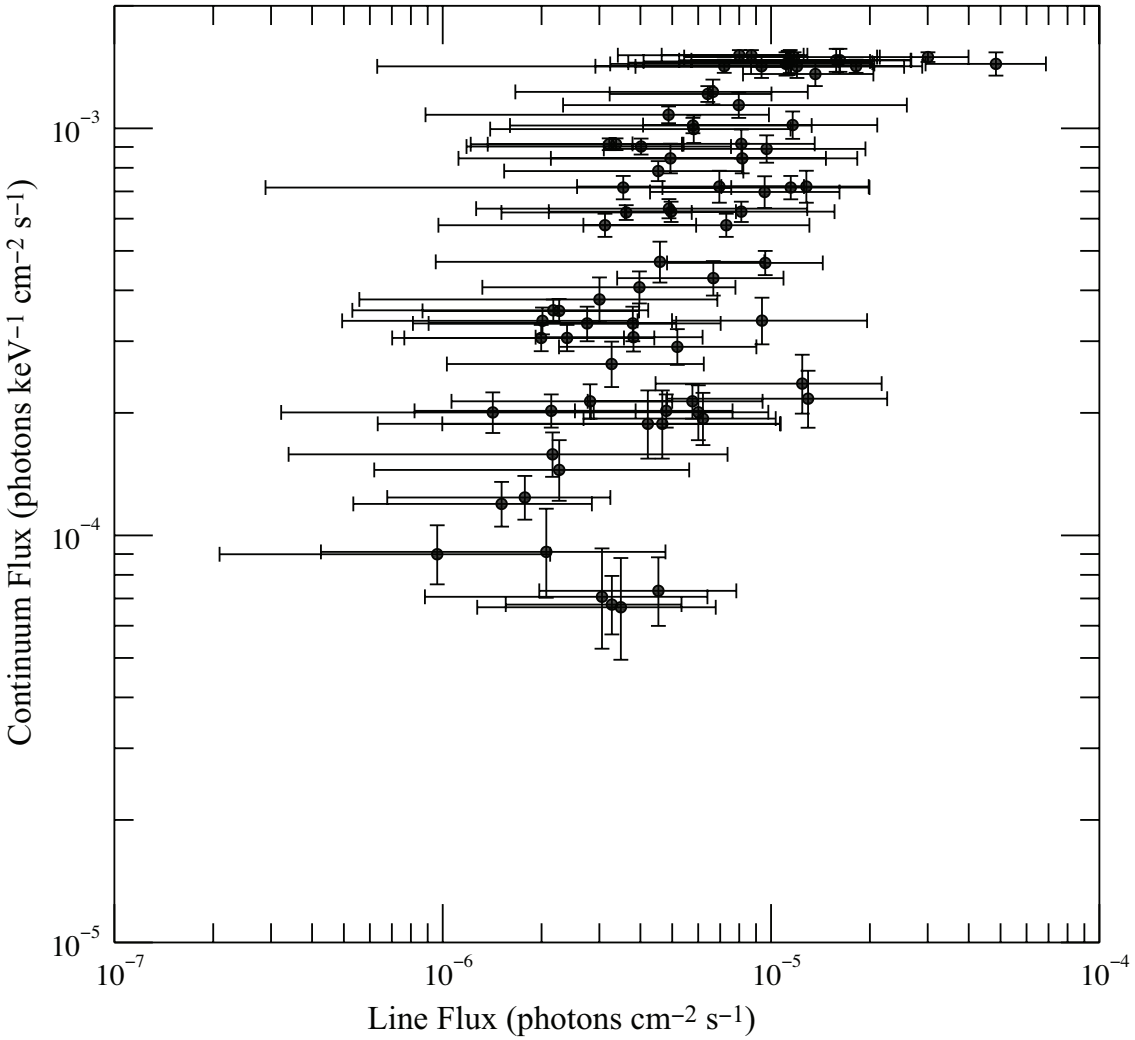

FIG. 8.— The flux of the Fe Kα line as a function of the continuum flux for Fe Kα lines detected at $> 90\%$ confidence in RXJ1131. The line flux is the normalization of the Gaussian line component of the best-fit model. The continuum flux is the normalization of the power-law component of the best-fit model calculated at 1 keV.

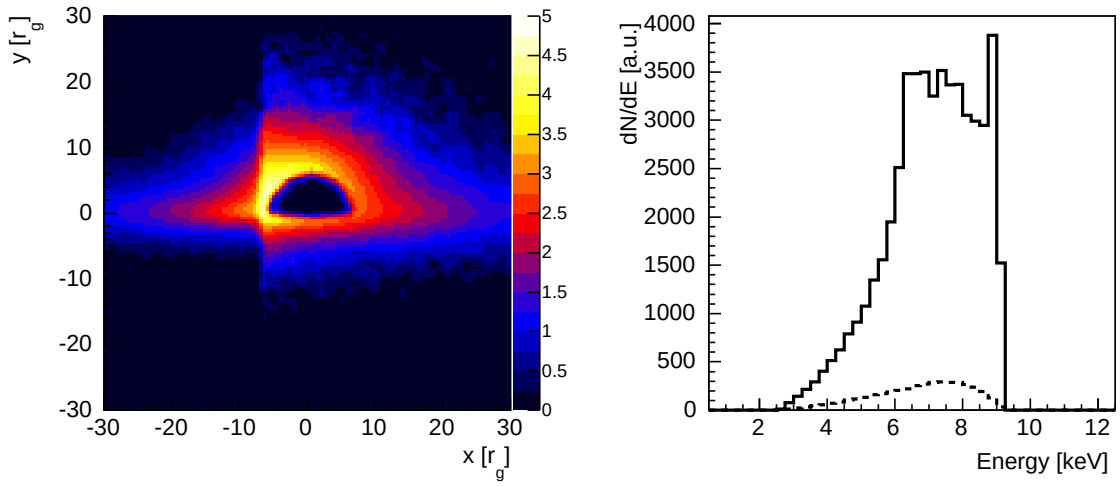

FIG. 9.— The left panel shows an image of the surface brightness of the Fe-Kα line emission as seen by an observer at 10^4 $r_{\rm g}$ and an inclination of $i = 82.5^\circ$ from a black hole of spin a=0.3 for a caustic crossing angle of $\theta_c = \pi/2$. The surface brightness scale is logarithmic with an arbitrary absolute scale. The surface brightness exhibits a left-right asymmetry owing to the motion of the accretion disk plasma towards to (left) or away from (right) the observer. The right panel shows the resulting energy spectrum of the Fe-Kα emission in the rest frame of the source.

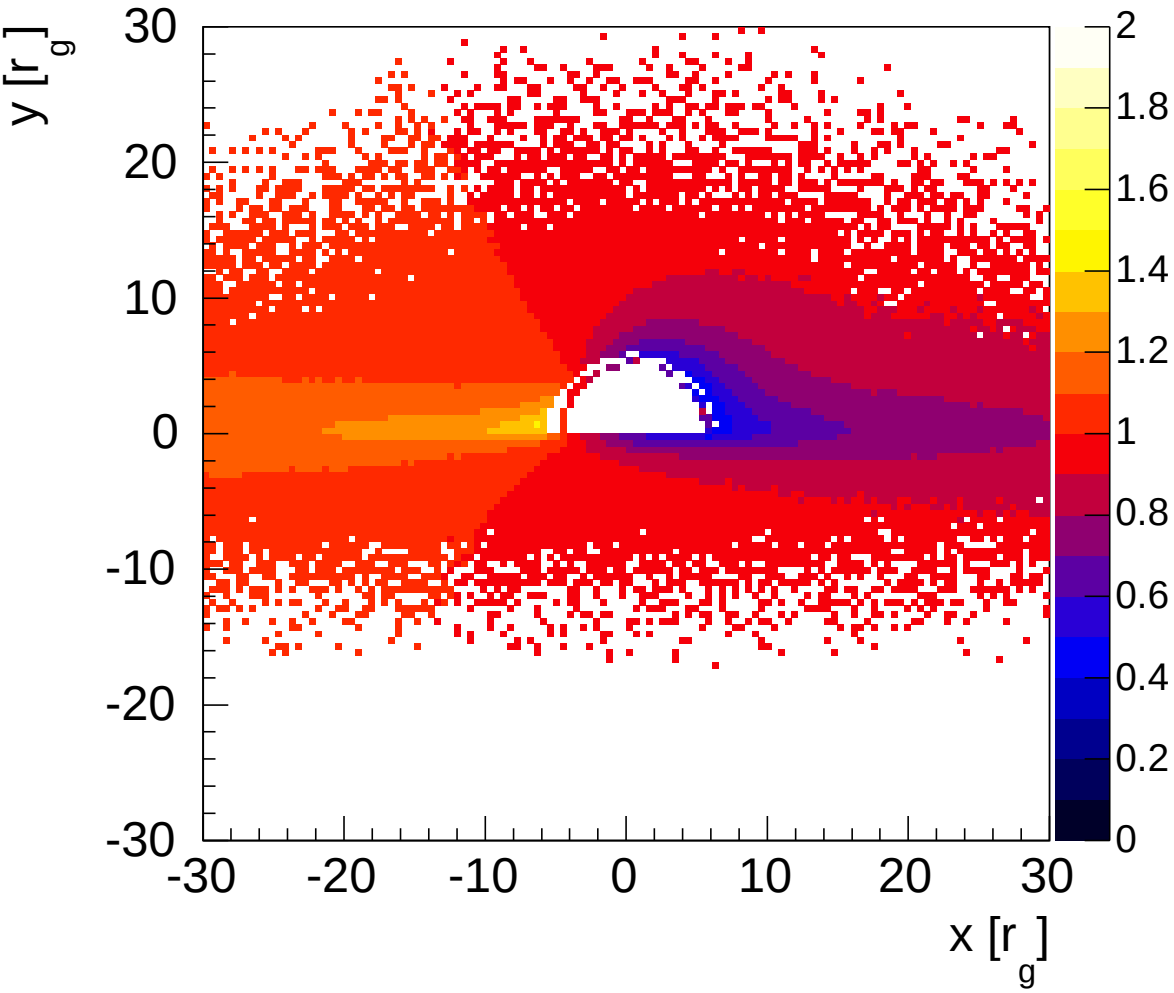

FIG. 10.— Map of the g-factors of the Fe-Kα emission originating in the accretion disk. The net g-factors result from the motion of the accretion disk plasma relative to the observer shown in Figure 9 and the propagation of the photon through the curved spacetime for the same parameters as were used in Figure 9.

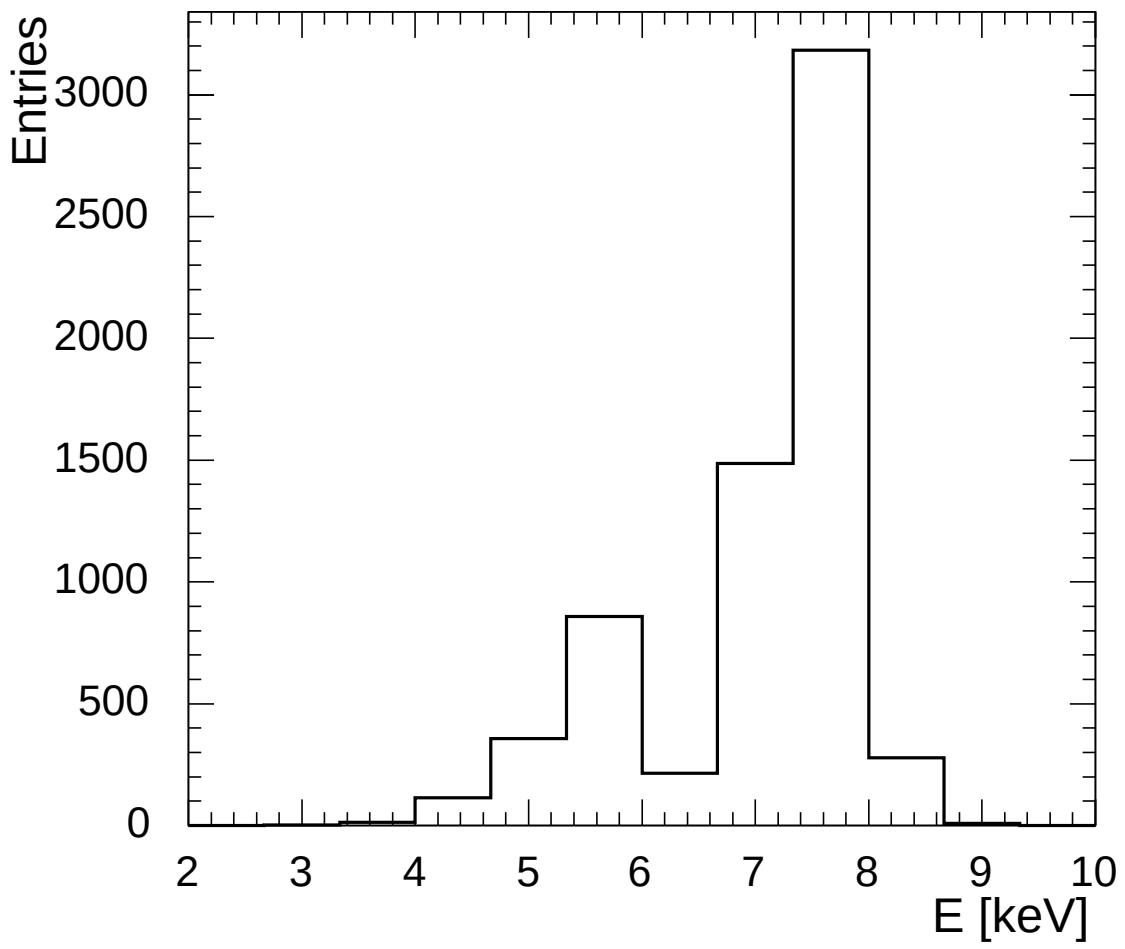

FIG. 11.— Simulated distribution of the *single and double peak* Fe line energies for a black hole with a spin of $a = 0.3$ seen at an inclination of $i = 82.5°$.

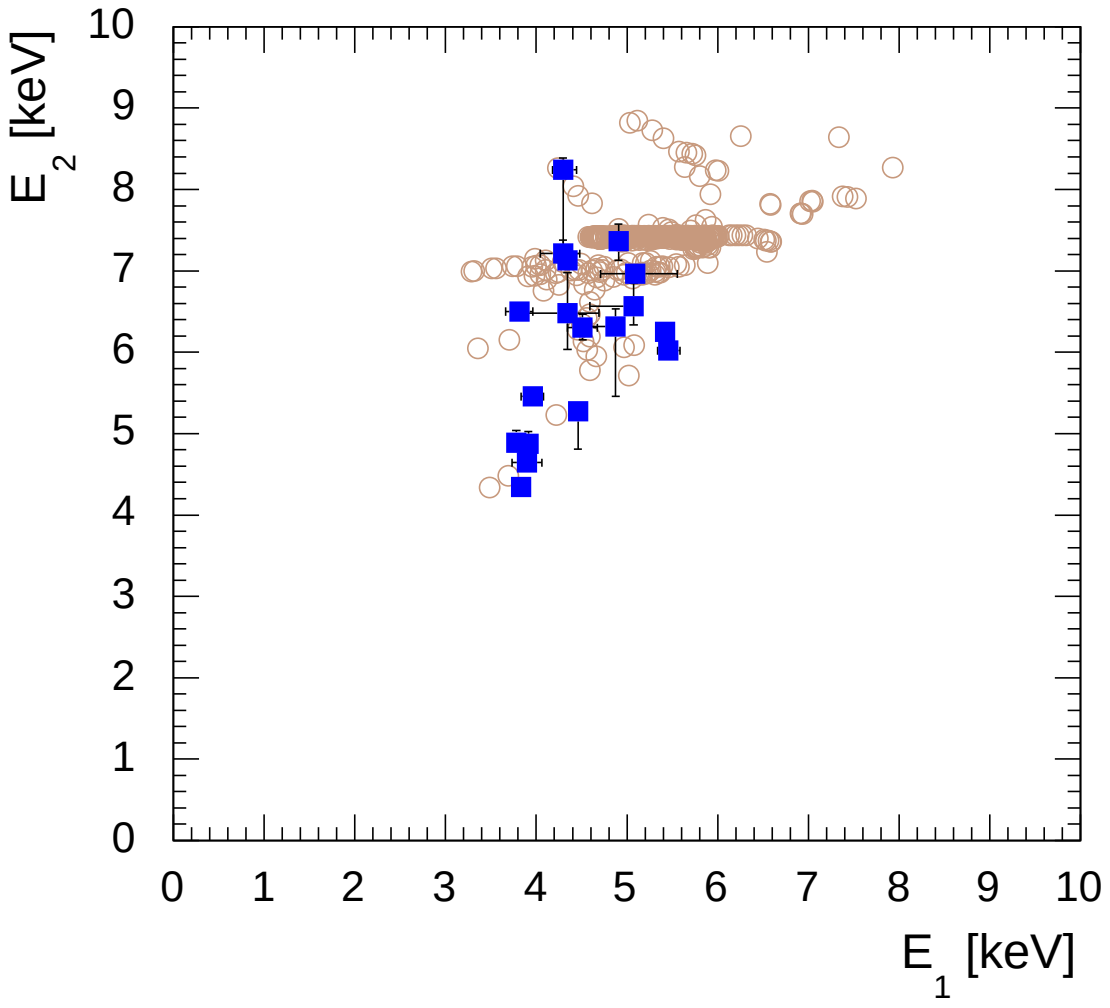

FIG. 12.— Scatter between the peak energies of simulated (open circles) and observed (solid squares) double-peaked line profiles. The simulations are for a black hole with a spin of $a = 0.3$ seen at an inclination of $i = 82.5°$.

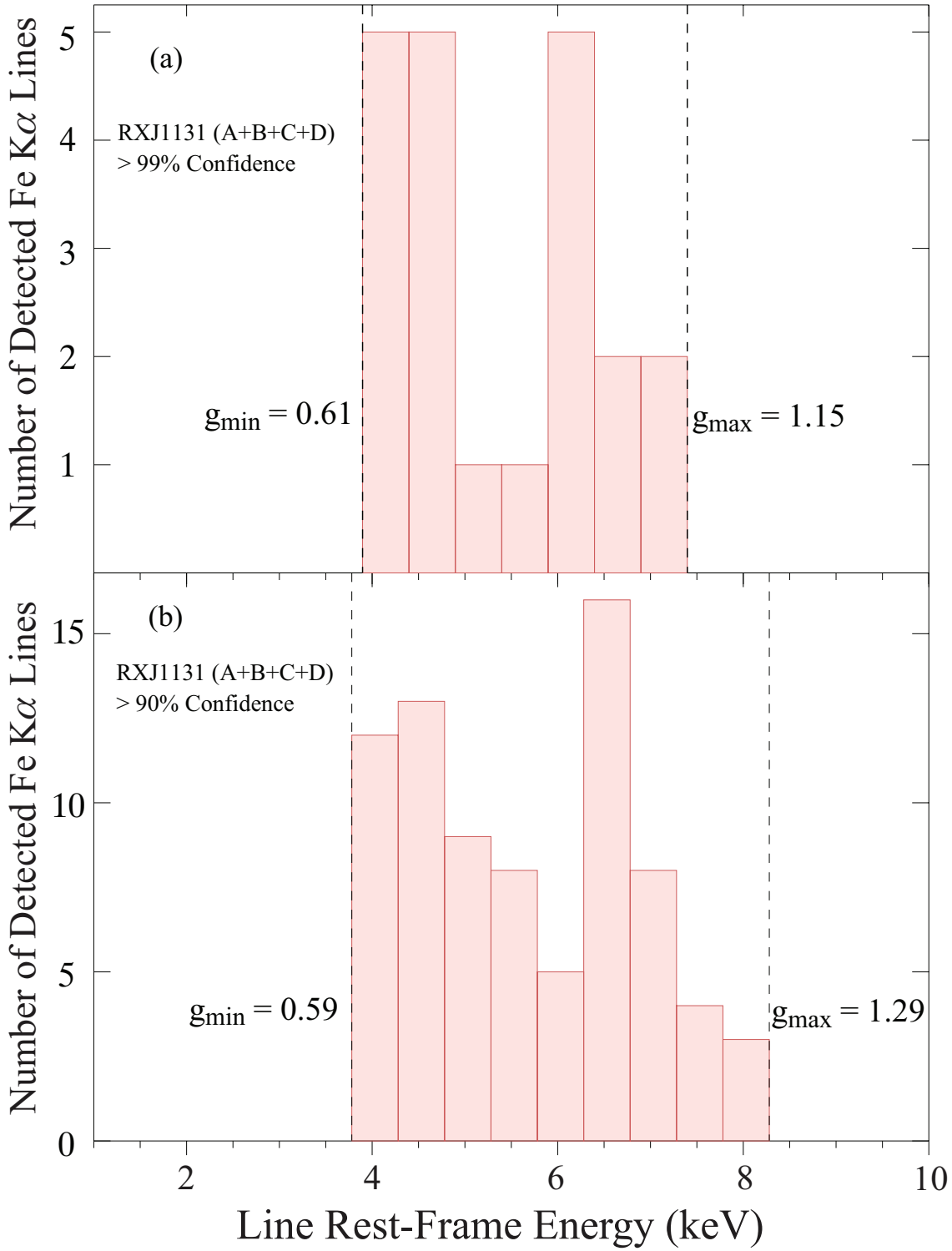

FIG. 13.— Distribution of the Fe Kα line energies for all images and all 38 epochs of data for RXJ1131. Only cases where the iron line is detected at > 99% (panel a) and at > 90% confidence (panel b) are shown. The vertical lines mark the extreme limits of the distribution used to determine upper limits on the ISCO and inclination angle.

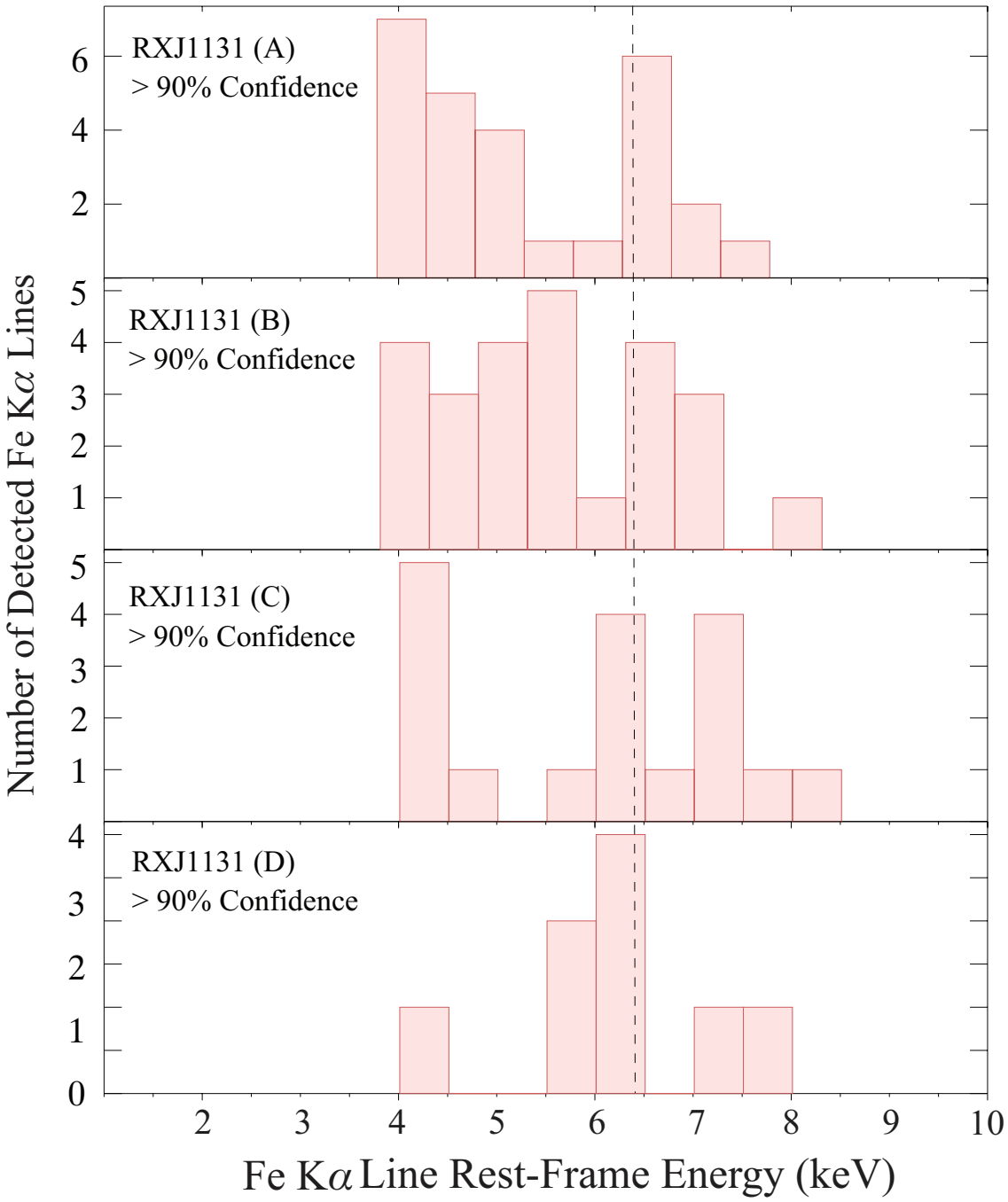

FIG. 14.— Distribution of the Fe Kα line energies for the individual images A, B, C, and D images and all 38 epochs of data for RXJ1131. Only cases where the iron line is detected at > 90% confidence are shown.

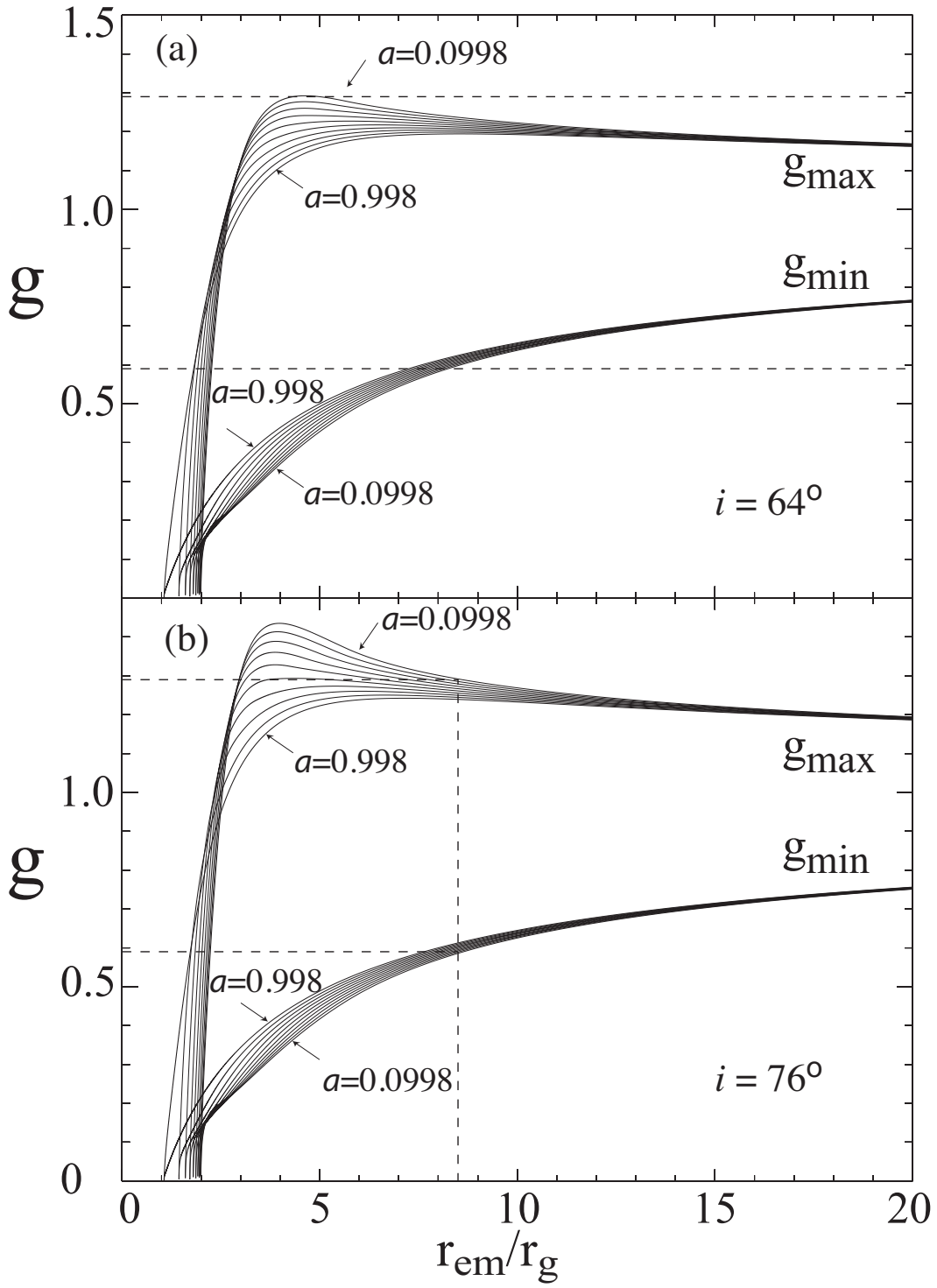

FIG. 15.— Extremal shifts of the Fe Kα line energy for spin values ranging between 0.098 and 0.998 in increments of 0.1. Horizontal lines represent the observed values of $g = E_{\rm obs}/E_{\rm rest}$ of the most redshifted and blueshifted Fe Kα lines from all 38 epochs and all images of RXJ1131. The extreme g values are for Fe Kα lines detected at $> 90\%$ confidence. (a) The extremal shifts for an inclination angle of $i = 64°$. (b) The extremal shifts for an inclination angle of $i = 76°$. The inner radius of the accretion disk is constrained to be $r_{\rm ISCO} < 8.5 r_{\rm g}$

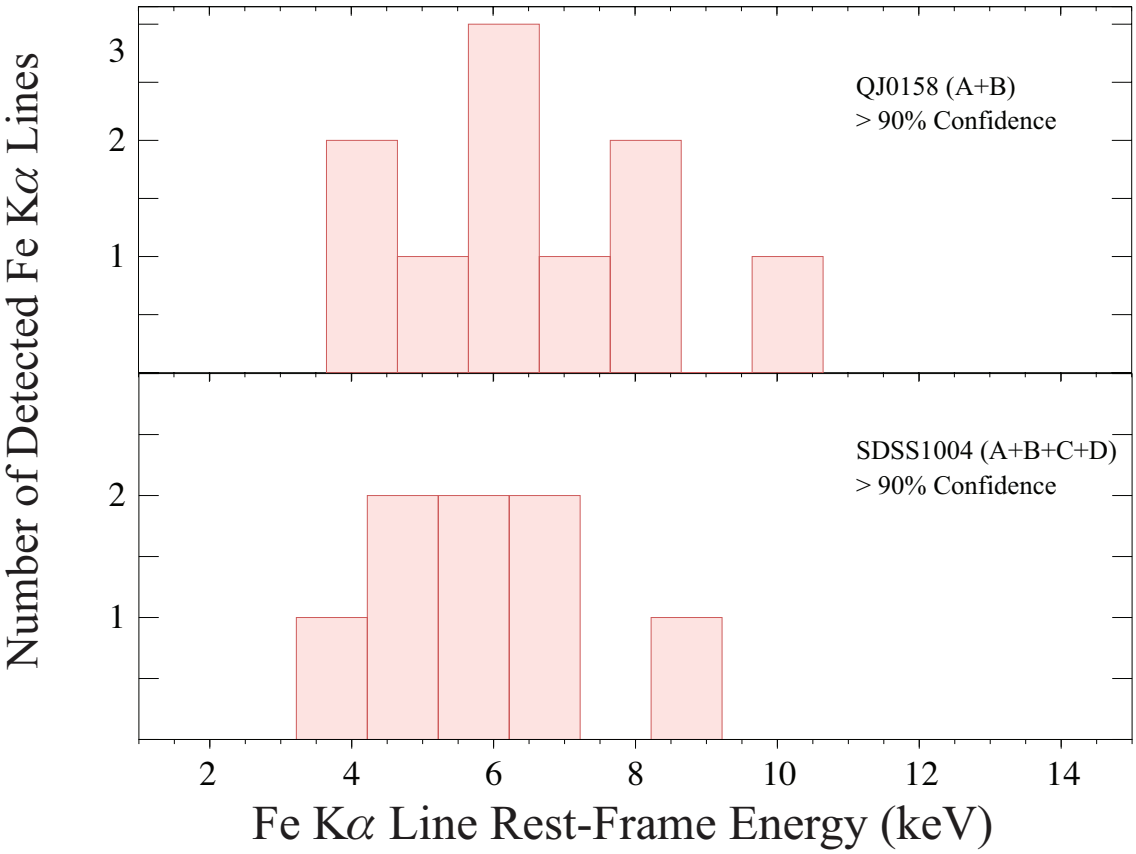

FIG. 16.— Distribution of the Fe Kα line energies for all images of QJ0158 (top, 12 epochs) and SDSS1004 (bottom, 10 epochs). Only cases where the iron line is detected at > 90% confidence are shown.

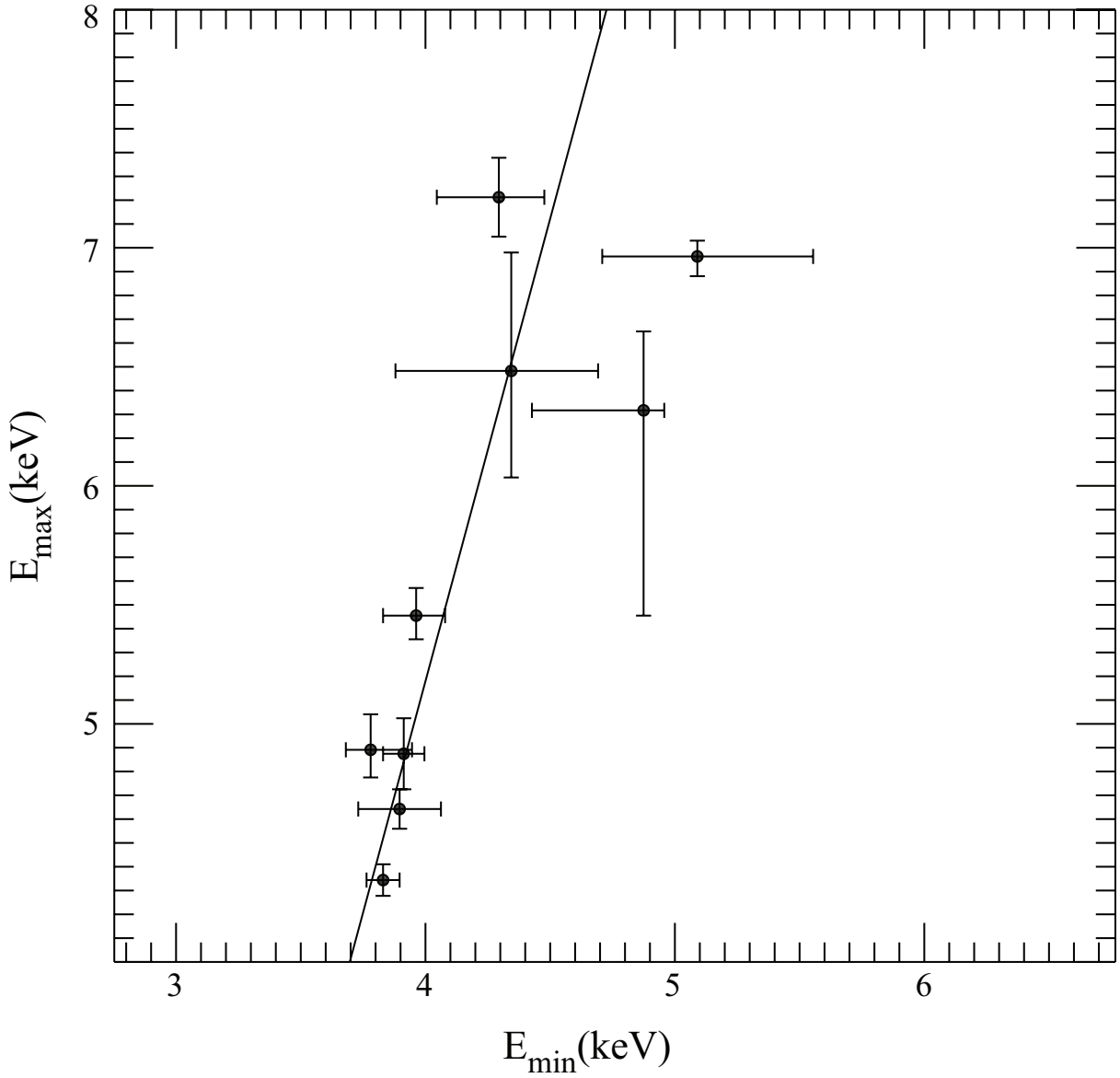

FIG. 17.— The rest-frame energies of the shifted double Fe lines detected in image A of RXJ1131 at the $> 90\%$ confidence level. We also show the straight-line least-squares fit to the data in the solid line.

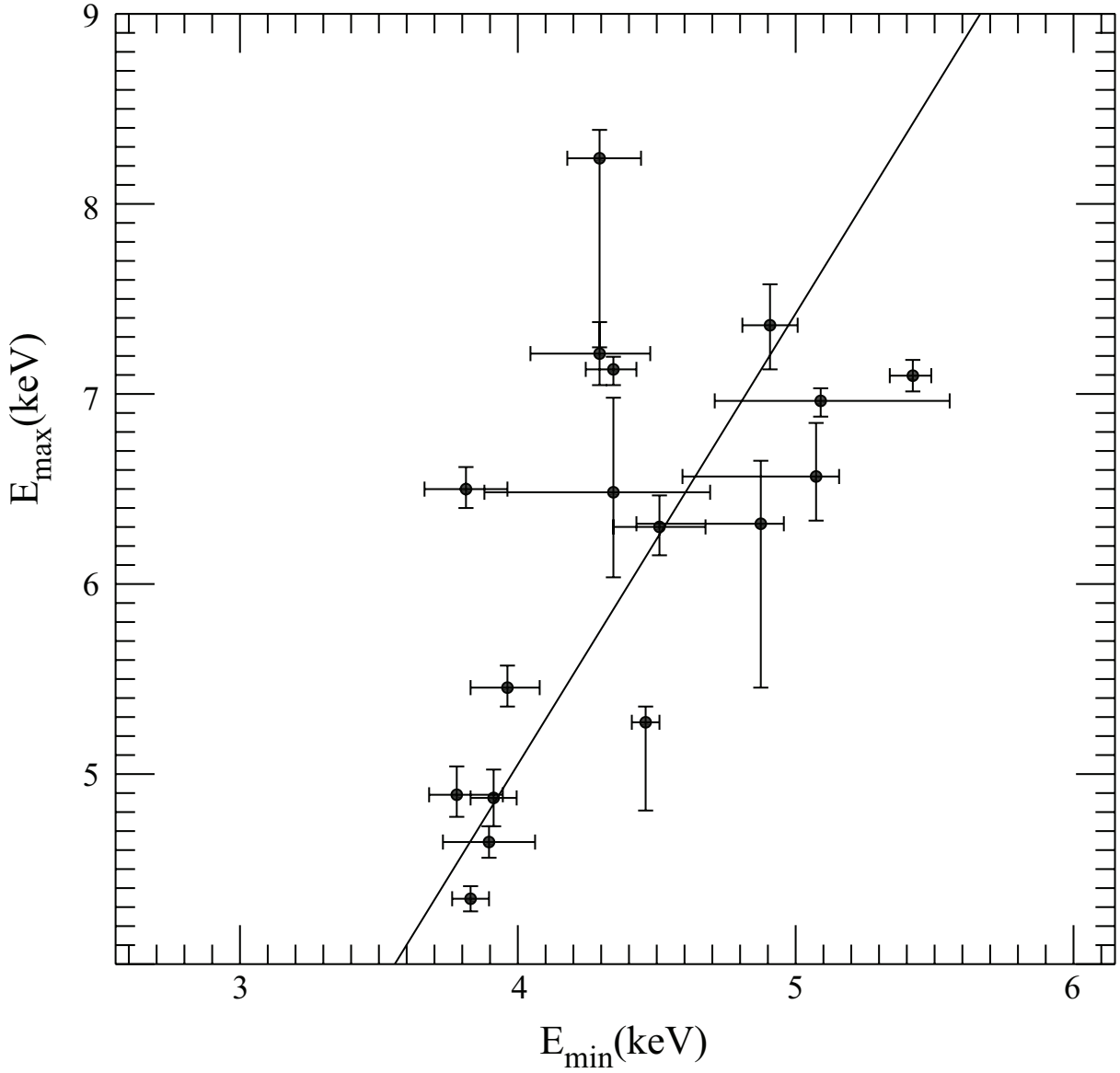

FIG. 18.— The rest-frame energies of the shifted double Fe lines detected in all images of RXJ1131 at the $> 90\%$ confidence level. We also show the straight-line least-squares fit to the data in the solid line.

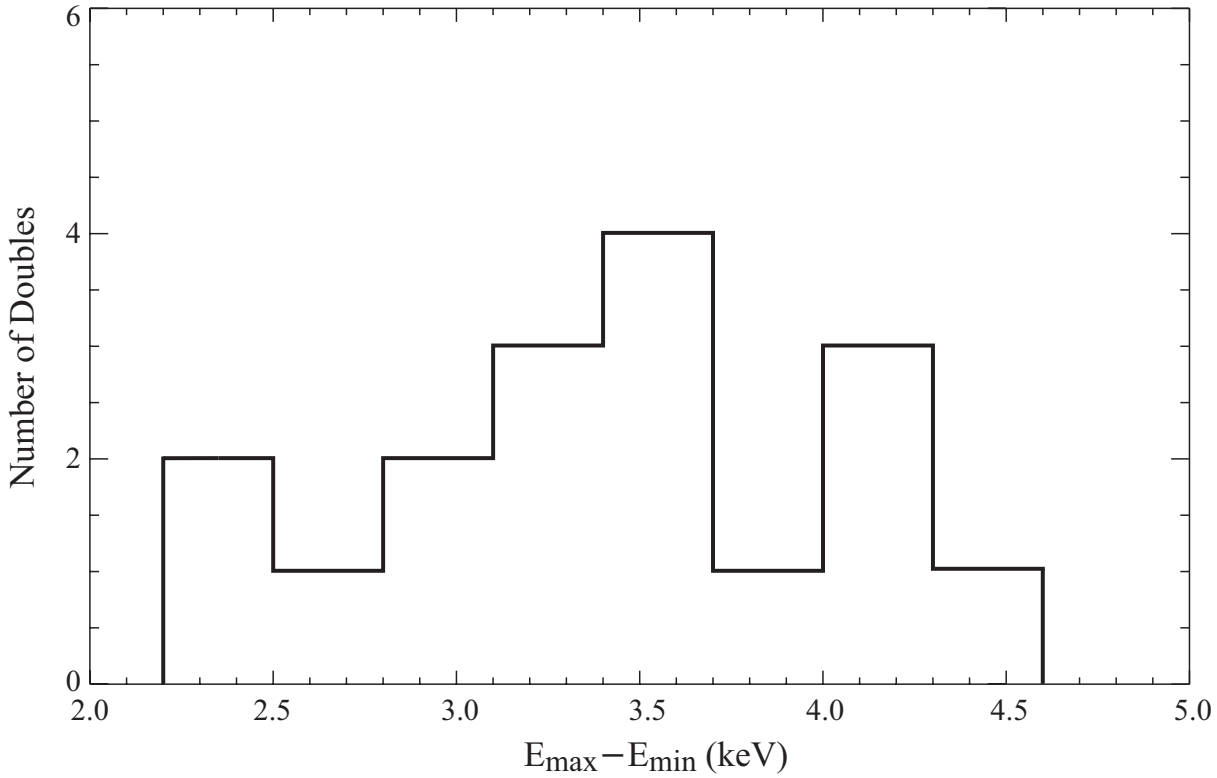

FIG. 19.— The observed distribution of the rest-frame energy separations for shifted double Fe lines detected in all images of RXJ1131 at the $> 90\%$ confidence level.